

Highly tunable nonlinear Hall effects induced by spin-orbit couplings in strained polar transition-metal dichalcogenides

Benjamin T. Zhou^{1,*}, Cheng-Ping Zhang^{1,†} and K. T. Law^{1,‡}

¹*Department of Physics, Hong Kong University of Science and Technology, Clear Water Bay, Hong Kong, China*

Recently, signatures of nonlinear Hall effects induced by Berry curvature dipoles have been found in atomically thin 1T'/T_d-WTe₂. In this work, we show that in strained polar transition-metal dichalcogenides(TMDs) with 2H-structures, Berry curvature dipoles created by spin degrees of freedom lead to strong nonlinear Hall effects. Under easily accessible uniaxial strain of order $\sim 0.2\%$, strong nonlinear Hall signals, characterized by Berry curvature dipole in the order of $\sim 1\text{\AA}$, arise in electron-doped polar TMDs such as MoSSe, which is easily detectable experimentally. Moreover, the magnitude and sign of the nonlinear Hall current can be easily tuned by electric gating and strain. These properties can be used to distinguish nonlinear Hall effects from classical mechanisms such as ratchet effects. Importantly, our system provides a potential scheme for building electrically switchable energy harvesting rectifiers.

I. INTRODUCTION

The study of Hall effects has been one of the central topics in condensed matter physics[1, 2]. Within the linear response regime, Hall effect arises only when time-reversal symmetry is broken[3, 4]. Recently, however, it was proposed by Sodemann and Fu[5] that Hall effects can occur in a wide class of time-reversal-invariant materials with broken spatial inversion symmetry. In such systems, the total Berry flux over the equilibrium distribution is zero due to time-reversal symmetry[1], while Berry curvatures can emerge locally in the Brillouin zone, with counter-propagating charge carriers having different Berry curvatures. Under an applied electric field, the current-carrying state maintains an imbalance between counter-propagating movers, which results in nonzero Berry curvature flux under proper symmetry conditions[6]. This leads to anomalous Hall currents which establish a Hall voltage in the steady state. As the electric field plays both roles of driving the system out of equilibrium and inducing anomalous velocities, the Hall current scales quadratically with the voltage bias. This special type of Hall effect is thus referred to as the nonlinear Hall effect(NHE). Due to the nonlinear current response, the NHE can convert oscillating electric fields into DC currents, a process known as rectification, which have potential applications for next-generation wireless and energy harvesting devices[7].

Nonlinear Hall response is characterized by the first-order moment of Berry curvatures over occupied states[5, 8, 9], called the Berry curvature dipole. In 2D systems, the Berry curvature dipole transforms as a pseudo-vector, thus the maximum symmetry allowed for a nonzero moment is a single mirror symmetry (mirror plane perpendicular to the 2D plane). Interestingly, atomically thin

transition-metal dichalcogenides(TMDs) with 1T'/T_d-structure, such as MoTe₂ and WTe₂, respect a single in-plane mirror symmetry[10], and nonzero Berry curvature dipoles are proposed to exist in these materials[11, 12]. Remarkably, two recent experiments have independently observed signatures of Hall effects in bilayer[13] and multi-layer WTe₂[14] in the absence of magnetic fields. Importantly, a quadratic scaling relation was found between the transverse voltage and the applied source-drain bias. While the observations are consistent with NHEs induced by Berry curvature dipoles[15], due to the relatively weak gate-dependence of Berry curvature dipoles in WTe₂[13], it remains experimentally challenging to directly rule out alternative trivial interpretations such as electron ratchet effects[5, 14, 16].

Besides 1T'/T_d-TMDs, it is known that TMDs with the usual 2H-structures also possess nontrivial Berry curvatures due to intrinsically broken inversion in orbital degrees of freedom[17, 18]. However, the three-fold(C_3) symmetry in 2H-TMDs forces the Berry curvature dipole to vanish[5]. Under applied strains that break the C_3 -symmetry, nonzero Berry curvature dipoles can arise in 2H-TMDs[5, 6, 11]. Unfortunately, the dipole moment in strained conventional 2H-TMDs is shown to be weak ($\sim 0.01\text{\AA}$)[5, 11], mainly due to the weak Berry curvatures generated by the huge Dirac mass ($\sim 1\text{ eV}$) in the orbital degrees of freedom[17].

Lately, it was proposed that in gated[19] or polar 2H-TMDs[20, 21], combined effects of Rashba and Ising spin-orbit couplings(SOCs) result in a different type of Berry curvature in spin degrees of freedom[22, 23]. Importantly, in 2H-TMDs the SOC-induced effect was found to be strong, which dominates over the conventional orbital effect and significantly changes the Berry curvatures in 2H-TMDs. However, the role of this SOC-induced Berry curvatures in creating nonlinear Hall effects in 2H-TMDs remains unknown.

In this work, we show that the large Berry curvatures induced by SOC lead to strong and gate-tunable nonlinear Hall effects(NHEs) in moly-based polar 2H-TMDs(Fig.1) such as MoSSe[24, 25]. With easily accessi-

*Correspondence author: bentzhou@ust.hk

These authors contributed equally to this work.

†These authors contributed equally to this work.

‡Correspondence author: phlaw@ust.hk

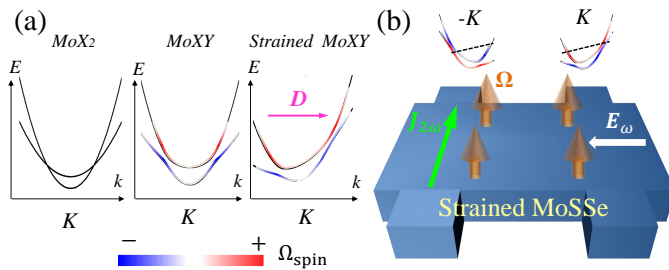


FIG. 1: Schematics for Berry curvature dipole in strained moly-based transition-metal dichalcogenides (TMDs). (a) Ω_{spin} near the conduction band minimum (CBM) at the $+K$ -point in 2H-TMDs. Left panel: in MoX_2 , spin-up and spin-down bands cross at finite momentum. Ω_{spin} is zero due to the absence of Rashba SOCs. Middle panel: in MoXY , Rashba SOCs cause anti-crossings within two spin-subbands, where hot spots of Ω_{spin} emerge at the same energy for left-movers and right-movers. Right panel: with $u_{xx} \neq 0$, anti-crossings for left-movers and right-movers are separated, creating nonzero Berry curvature dipole \mathbf{D} in MoXY . (b) Under electric field \mathbf{E}_ω with frequency ω , the non-equilibrium state in strained MoSSe gains net Berry curvature flux (denoted by the orange arrows), which combines with \mathbf{E}_ω to generate nonlinear Hall current signified by second-harmonic component $\mathbf{J}_{2\omega}$.

ble low carrier density and weak uniaxial strain of order $\sim 0.2\%$, pronounced nonlinear Hall signals arise in polar TMDs characterized by Berry curvature dipoles on the order of $\sim 1\text{\AA}$ (Fig.3), comparable to the optimal values observed recently in $1\text{T}'_d\text{-WTe}_2$ [13, 14].

Importantly, the magnitude and sign of nonlinear Hall signals in strained polar TMDs change dramatically upon gating the Fermi level $\sim 10 - 20$ meV away from the conduction band minimum (Fig.2(c)). Therefore, nonlinear Hall effects in strained polar TMDs generally exhibit a stronger gate-dependence than $1\text{T}'_d\text{-WTe}_2$ [13], which can be easily detected in Hall measurements with moderate gating. We further point out that the gate-sensitive NHE in strained polar TMDs provides a promising scheme for realising electrically switchable rectifiers for wireless energy harvesting devices. The highly gate-tunable NHE in strained polar TMDs also serves as a distinctive and accessible experimental signature of Berry curvature dipoles, which distinguishes itself from nonlinear effects due to trivial classical mechanisms [5, 14, 16].

II. RESULTS

A. Effective model Hamiltonian of strained MoSSe

Throughout this work, we consider MoSSe as a specific example of polar TMDs, which has been successfully fabricated in recent experiments [24, 25]. However, our prediction generally applies to the whole class of moly-based polar TMDs MoXY , ($X \neq Y$) [20, 21].

To distinguish the two types of Berry curvatures in 2H-

TMDs originating from orbital/spin degrees of freedom, we use the notations $\Omega_{orb}/\Omega_{spin}$ to denote the conventional Berry curvatures/the SOC-induced Berry curvatures.

To describe the essential mechanism behind the emergence of Berry curvature dipole, we first construct an effective Hamiltonian for n -type (electron-doped) strained polar TMDs. The crystal structure of a generic polar TMD is almost the same as a usual 2H-TMD except that the triangularly arranged transition-metal (M) atoms are sandwiched by two different layers of chalcogen atoms [20, 21, 24, 25]. Thus, the out-of-plane mirror symmetry (mirror plane parallel to the 2D plane of M-atoms), which is generally respected by usual 2H-TMDs, is intrinsically broken. The resultant symmetry group of MoSSe is the product group of the C_{3v} point group and time-reversal symmetry \mathcal{T} .

Near the conduction band minimum (CBM) at the K -points, electrons in polar TMDs originate predominantly from the d_{z^2} -orbitals of the M-atoms [26]. Under the basis formed by spins of d_{z^2} -electrons, the unstrained effective Hamiltonian of MoSSe can be written as [22, 23, 27]:

$$H_0 = \xi_{\mathbf{k}} \sigma_0 + \alpha_{so} (k_y \sigma_x - k_x \sigma_y) + \epsilon \beta_{so}(\mathbf{k}) \sigma_z. \quad (1)$$

Here, σ_i , $i = 0, x, y, z$ denotes the usual Pauli matrices acting on the spin degrees of freedom. $\xi_{\mathbf{k}} = \frac{|\mathbf{k}|^2}{2m^*} - \mu$ denotes the kinetic energy term, m^* is the effective mass of the electron band, μ is the chemical potential, $\epsilon = \pm$ is the valley index.

The $\beta_{so}(\mathbf{k})$ -term refers to the Ising SOC which originates from the atomic spin-orbit coupling as well as the breaking of an in-plane mirror symmetry [28–31]. In previous studies on 2H-TMDs, the Ising SOC was usually treated as a constant near the K -points [22, 23, 27]. However, in realistic band structures of conventional moly-based 2H-TMDs, spin-up and spin-down bands cross at finite momentum k_0 (left panel of Fig.1(a)) [26]. This indicates a sign change in the Ising SOC term at the crossing, which can be accounted by quadratic corrections in \mathbf{k} : $\beta_{so}(\mathbf{k}) = \beta_0 + \beta_1 k^2$, with $\text{sgn}(\beta_0) \text{sgn}(\beta_1) < 0$. The crossing for spin-up and spin-down bands occurs at $k_0 = \pm \sqrt{-\beta_0/\beta_1}$. The α_{so} -term is known as the Rashba SOC [32], which arises in MoSSe due to intrinsically broken out-of-plane mirror symmetry.

Interestingly, per each K -valley the coexistence of Ising and Rashba SOCs results in a modified massive Dirac Hamiltonian $H_0 = \xi_{\mathbf{k}} \sigma_0 + \mathbf{d}_\epsilon(\mathbf{k}) \cdot \boldsymbol{\sigma}$, which is reminiscent of the well-known BHZ model for a 2D topological insulator [33] with $\mathbf{d}_\epsilon(\mathbf{k}) = [\alpha_{so} k_y, -\alpha_{so} k_x, \epsilon(\beta_0 + \beta_1 k^2)]$ except that the kinetic $\xi_{\mathbf{k}}$ -term bends the electron bands up, with two non-degenerate spin-subbands (Fig.1(a)). The energy spectra for the upper/lower spin subbands are given by: $E_{\pm}(\mathbf{k} + \epsilon \mathbf{K}) = \xi_{\mathbf{k}} \pm \epsilon |\mathbf{d}(\mathbf{k})|$ where $|\mathbf{d}(\mathbf{k})| = \sqrt{\alpha_{so}^2 k^2 + (\beta_0 + \beta_1 k^2)^2}$. The Berry curvatures of the two

subbands are given by[34, 35]:

$$\begin{aligned}\Omega_{spin,\pm}(\mathbf{k} + \epsilon\mathbf{K}) &= \mp \frac{1}{2} \hat{\mathbf{d}}_\epsilon(\mathbf{k}) \cdot \left(\frac{\partial \hat{\mathbf{d}}_\epsilon}{\partial k_x} \times \frac{\partial \hat{\mathbf{d}}_\epsilon}{\partial k_y} \right) \quad (2) \\ &= \mp \frac{1}{2} \epsilon \frac{\alpha_{so}^2 (\beta_0 - \beta_1 k^2)}{|\mathbf{d}(\mathbf{k})|^3}.\end{aligned}$$

Note that the nontrivial $\Omega_{spin,\pm}(\mathbf{k})$ requires the presence of both Ising and Rashba SOCs. In the absence of Rashba SOCs, the upper and lower subbands consist of decoupled spin-up and spin-down states and no Ω_{spin} can be generated (left panel of Fig.1(a)). In moly-based polar TMDs, the Rashba SOC hybridizes the spin-up and spin-down bands and causes an anti-crossing within the spin subbands (middle panel of Fig.1(a)). In particular, hot spots of Ω_{spin} emerge in the vicinity of the crossing points k_0 , with their signs being opposite in upper and lower subbands. Given realistic parameters, Ω_{spin} near its hot spots has a magnitude $|\Omega_{spin}| \gg 100 \text{ \AA}^{-2}$ (see Appendix A for details).

Despite the large Ω_{spin} , the Berry curvature dipole remains zero in unstrained MoSSe due to the three-fold(C_3) symmetry[5]. Physically, the Berry curvature dipole measures the gain in total Berry curvature flux in the current-carrying state[6]. When C_3 -symmetry is present, the Berry flux from left-movers is always equal to that from right-movers on the Fermi surface (middle panel of Fig.1(a)). Thus, the imbalance between left-movers and right-movers established by a source-drain bias leads to no gain in total Berry flux up to the lowest order correction.

To break the C_3 -symmetry, one feasible way is to introduce uniaxial strains[5, 6, 11]. Following the scheme developed in the recent work[36], effects of strains in 2D TMDs can be modelled by classifying the strain-field tensor $\overleftrightarrow{\mathbf{u}}_{ij} = (\partial_i u_j + \partial_j u_i)/2$, ($i, j = x, y$) according to the irreducible representations of the C_{3v} point group of polar TMDs. In total, $\overleftrightarrow{\mathbf{u}}$ has three effective independent components: (i) the trace scalar $u_0 \equiv (u_{xx} + u_{yy})$; and (ii) the doublet $\{u_1, u_2\} \equiv \{2u_{xy}, u_{xx} - u_{yy}\}$ that transforms as a polar vector. Details of the symmetry properties of u_0, u_1, u_2 are presented in Appendix A.

To capture the essential physics, we consider strain effects on spin-independent terms only, which has no contributions to Berry curvatures. This approximation is based on the observation that the coupling strength between the spin-independent terms and strain-field $\overleftrightarrow{\mathbf{u}}$ have an energy scale $\sim 1 \text{ eV}$ [36], which is far greater than spin-orbit couplings on the scale of a few to tens of meVs. Up to linear order terms in \mathbf{k} , the effective strained Hamiltonian compatible with the $C_{3v} \otimes \mathcal{T}$ symmetry group is given by:

$$\begin{aligned}H_{strain} &= [\gamma u_0 + \epsilon \delta (u_1 k_y - u_2 k_x)] \sigma_0, \quad (3) \\ H_{eff} &= H_0 + H_{strain},\end{aligned}$$

where H_{eff} is the total effective Hamiltonian, and γ, δ are effective strained parameters. Considering uniaxial

strains in the x -direction: $u_{xx} \neq 0$ and $u_{xy} = u_{yy} = 0$, the strained energy spectra are given by: $E'_\pm(\mathbf{k}) = u_{xx}(\gamma - \epsilon \delta k_x) + \xi_{\mathbf{k}} \pm |\mathbf{d}_\epsilon(\mathbf{k})|$. Clearly, the δ -term breaks the C_3 -symmetry by shifting the band minimum along the k_x direction[5]. As a result, the two pairs of Berry curvature hot spots associated with the left-movers and right-movers are energetically separated(Fig.1(a), right panel). For Fermi level close to one of these separated hot spots, an applied bias in the x -direction creates an imbalance between left-movers and right-movers, and the system acquires nonzero out-of-plane Berry curvature flux in the current-carrying state(orange arrows in Fig.1(b)). This current-induced Berry flux then combines again with the applied field to generate currents in transverse y -direction as shown schematically in Fig.1(b).

B. Large and gate-tunable Berry curvature dipoles in strained MoSSe

Having established how Ω_{spin} combines with uniaxial strains to create Berry curvature dipoles, we now go beyond the effective two band model and study the nonlinear Hall effect in strained MoSSe under realistic situations. Using a six-orbital tight-binding model for strained TMDs[26, 36], we take both Ω_{spin} and Ω_{orb} into account and study the Berry curvature as well as its dipole moment in electron-doped strained MoSSe. As we are about to show, the dominance of Ω_{spin} over Ω_{orb} , together with uniaxial strains, leads to strong and highly gate-tunable nonlinear Hall effects in strained MoSSe. Details of the tight-binding Hamiltonian are presented in Appendix C.

As we discussed in the last section, the Berry curvature dipole measures the lowest-order correction in total Berry curvature flux in the non-equilibrium state. This physical meaning is revealed by its formal expression [5, 13]:

$$\begin{aligned}D_\alpha &= - \sum_n \int \frac{d^2 \mathbf{k}}{(2\pi)^2} (\partial_{k_\alpha} f_n) \Omega_n(\mathbf{k}) \quad (4) \\ &= \sum_n \int \frac{d^2 \mathbf{k}}{(2\pi)^2} v_{n,\alpha}(\mathbf{k}) \delta_F(E_n - E_F) \Omega_n(\mathbf{k}).\end{aligned}$$

Here, D_α denotes the α -component of the Berry curvature dipole \mathbf{D} , with $\alpha = x, y$. f_n, Ω_n refer to the equilibrium distribution function and Berry curvature of bands indexed by n . $v_{n,\alpha} = \partial E_n / \partial k_\alpha$ is the band velocity and $\delta_F(E - E_F) = -\partial f / \partial E = [4k_B T \cosh^2(\frac{E - E_F}{2k_B T})]^{-1}$ mimics a delta-function with its maximum value $\delta_F^{max} = 1/4k_B T$ centered at E_F .

In general, the Berry curvature dipole in a polar TMD has contributions from both K and $-K$ valleys. Due to time-reversal symmetry, $v_{n,\alpha}(\mathbf{k} + \mathbf{K}) = -v_{n,\alpha}(-\mathbf{k} - \mathbf{K})$, $\Omega_n(\mathbf{k} + \mathbf{K}) = -\Omega_n(-\mathbf{k} - \mathbf{K})$. Thus, contributions from the two K valleys are equal, which allows us to consider the $+K$ -valley only for the simplicity of our following discussions.

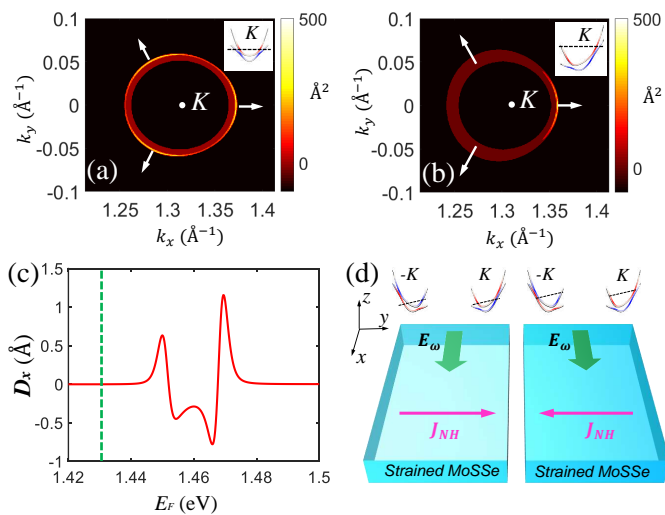


FIG. 2: Realistic Berry curvature and its dipole moment in MoSSe. Berry curvature profiles on the Fermi surface contour in (a) unstrained MoSSe, and (b) strained MoSSe. Contributions from both spin subbands are included. Berry curvatures are weighted by the normalized delta function δ_F/δ_F^{max} , with temperature $T = 10K$. In-sets in (a)-(b): schematics for locations of E_F in each case. Colors of the bands indicate the Berry curvature values. (c) Berry curvature dipole D_x versus Fermi energy E_F in strained MoSSe (red solid line) calculated from realistic tight-binding model under uniaxial strain $u_{xx} = 4\%$. The green dashed line indicates the location of band minimum. (d) Schematics for strong gate-dependence of nonlinear Hall effects in strained MoSSe. By gating E_F across the band anti-crossing associated with the right-movers in the $+K$ -valley, the nonlinear Hall current J_{NH} switches sign.

As explained previously, Berry curvature dipoles vanish in MoSSe in the absence of strains. Since the Berry curvature dipole is a Fermi liquid property[5], this symmetry property can be explicitly revealed by the Berry curvature profile on the Fermi surface contour of an unstrained MoSSe. Without loss of generality, we consider E_F lying slightly above the Berry curvature hot spot in the upper band (in-set of Fig.2(a)). Apparently, due to the C_3 -symmetry, Berry curvatures of three-fold-related momentum states $\{\mathbf{k}, C_3\mathbf{k}, C_3^2\mathbf{k}\}$ must satisfy: $\Omega_n(\mathbf{k}) = \Omega_n(C_3\mathbf{k}) = \Omega_n(C_3^2\mathbf{k})$ (Fig.2(a)), and their band velocities (indicated by arrows in Fig.2(a)) sum to zero: $\sum_{j=1}^3 v_{n,\alpha}(C_3^{j-1}\mathbf{k}) = 0$. These symmetry constraints force contributions from left-movers and right-movers to cancel each other, leading to vanishing dipole moments in Eq.4.

However, due to the fact that the total Berry curvature Ω_{tot} near the band anti-crossing points is approximately a sum of Ω_{spin} and Ω_{orb} (see Appendix D for details), the dominance of Ω_{spin} over Ω_{orb} implies that the behavior of Ω_{tot} is essentially governed by Ω_{spin} . Therefore, Ω_{tot} in both upper and lower subbands exhibit similar nonuniform momentum-space profiles as Ω_{spin} (see Appendix D for details), with hot spots emerging near the

anti-crossing points (shown schematically in the in-set of Fig.2(a)).

Importantly, Ω_{tot} in the upper and lower subbands have opposite signs[22](indicated by the red/blue colors in the in-sets of Fig.2(a)-(b)). While this generally leads to partial cancellation within the two subbands, it is important to note that for Fermi level located slightly above(below) the anti-crossing points, the Fermi momentum of the upper(lower) subband is closer to the hot spots, thus its Berry curvature contribution dominates over the other subband at the Fermi energy, leading to a large net Berry flux per each K -valley on the Fermi surface contour. For instance, for Fermi level slightly above the band anti-crossing, the upper subband dominates, with the overall sign of the Berry curvature being positive around K (Fig.2(a)).

Under uniaxial strains, the anti-crossings associated with the left-movers and right-movers are energetically separated. Thus, for Fermi levels located slightly above or below one of the separated anti-crossing points, there generally exists a huge difference between Berry curvature contributions from left-movers and right-movers. To be specific, we plot the Berry curvature profile on the Fermi surface contour of strained MoSSe under $u_{xx} = 4\%$, with E_F lying slightly higher than the anti-crossing point associated with the right-movers (in-set of Fig.2(b)). Apparently, contributions from the right-movers far exceed those from left-movers, with the overall sign being positive due to the dominance of the upper band (Fig.2(b)). In this case, the system gains a large amount of Berry flux as the left-movers are pumped by the voltage bias to the right or vice versa, which signifies a large Berry curvature dipole.

Moreover, since the upper/lower subband dominates for Fermi levels above/below the anti-crossing, the net Berry curvature on the Fermi surface changes sign as the Fermi level is gated across these anti-crossing points, indicating a sign switch in the Berry curvature dipole (Eq.4). The Berry curvature dipole D_x as a function of E_F under $u_{xx} = 4\%$ is plotted in Fig.2(c). At the band minimum(indicated by green dashed line in Fig.2(c)), the Berry curvature dipole is zero due to the vanishing band velocity. As E_F increases, the anti-crossing associated with the left-movers is first accessed. Evidently, D_x changes from positive to negative values as E_F goes across the anti-crossing. This gives rise to a peak followed by a dip as shown in the $D_x - E_F$ curve (E_F in the range 1.44 ~ 1.46 eV in Fig.2(c)).

By further raising the Fermi level, one reaches the anti-crossing associated with the right-movers. However, since the band velocities of right-movers and left-movers are opposite to each other, D_x changes sign in an opposite manner according to Eq.4, *i.e.*, from negative to positive values as E_F sweeps across the anti-crossing. This leads to a dip followed by a peak in the $D_x - E_F$ curve (E_F in the range 1.46 ~ 1.48 eV in Fig.2(c)).

Consider a strained MoSSe with coordinates defined in Fig.2(d)), an oscillating electric field with frequency

ω : $\mathbf{E}_\omega(t) = \text{Re}\{\mathcal{E}_x e^{i\omega t}\}\hat{x}$ in the x -direction can drive a second-harmonic transverse current along y -direction in strained MoSSe(Fig.1(b)), with the current amplitude given by[5]:

$$j_y^{2\omega} = -\frac{e^3 \tau \mathcal{E}_x^2}{2(1 + i\omega\tau)} D_x, \quad (5)$$

where τ is the relaxation time. As $j_y^{2\omega}$ is proportional to D_x , the nonlinear Hall current in MoSSe also changes sign upon gating the Fermi level across the anti-crossing. This sign switch occurs within a narrow Fermi level range $\Delta E_F \sim 10$ meV(Fig.2(d)) and thus can be easily controlled by moderate gating. The second-harmonic Hall current $j_y^{2\omega}$ establishes an AC Hall voltage with frequency 2ω , which can be readily detected by usual Hall bar geometry as in recent experiments on bilayer and multilayer WTe₂[13, 14].

C. Strain-gate map of nonlinear Hall response in MoSSe

In this section, we systematically demonstrate how the gate-dependence of NHEs in MoSSe evolves under uniaxial strain u_{xx} ranging from 0% up to 4%(Fig.3a). Importantly, we show that a tiny amount of uniaxial strain $u_{xx} \sim 0.2\%$ is sufficient for creating sizeable Berry curvature dipoles of the order $\sim 1\text{\AA}$ (Fig.3b).

As we explained in subsection A, the uniaxial strain plays the essential role of breaking the C_3 -symmetry and gives rise to nonzero Berry dipoles in MoSSe. In particular, large Berry dipoles in MoSSe are physically established by the strain-induced energy separation of Berry curvature hot spots associated with left-movers and right-movers(Fig.1a). Thus, as one gradually turns on the uniaxial strain, the Berry curvature hot spots associated with left-movers and right-movers start to get separated in energy and nonzero Berry dipole D_x emerges.

A complete 2D map of D_x as a function of Fermi energy E_F and uniaxial strain u_{xx} is shown in Fig.3a, with the black solid line indicating locations of the conduction band minimum(CBM). At $u_{xx} = 0\%$, the C_3 -symmetry in MoSSe is respected, with $D_x = 0$ in all ranges of E_F . As u_{xx} is turned on, nonzero Berry dipoles D_x start to emerge. Notably, the band anti-crossing points providing Berry curvature hot spots(Fig.1a) are generically located ~ 20 meVs away from the CBM. As E_F accesses these hot spots, it is evident from Fig.3a that pronounced signals of D_x of the order $\sim 1\text{\AA}$ readily appear under very weak uniaxial strains $u_{xx} \sim 0.2\%$.

To understand why such strong Berry dipoles can be induced by weak strains, we study the evolutionary behavior of D_x under strains by plotting D_x as a function of E_F at various fixed strains: $u_{xx} = 0.2\%, 1.2\%, 2.2\%, 3.2\%$, as shown in Fig.3b-e. The black double arrows in each case measure the energy separation between the lowest- and highest-lying Berry curvature hot spots.

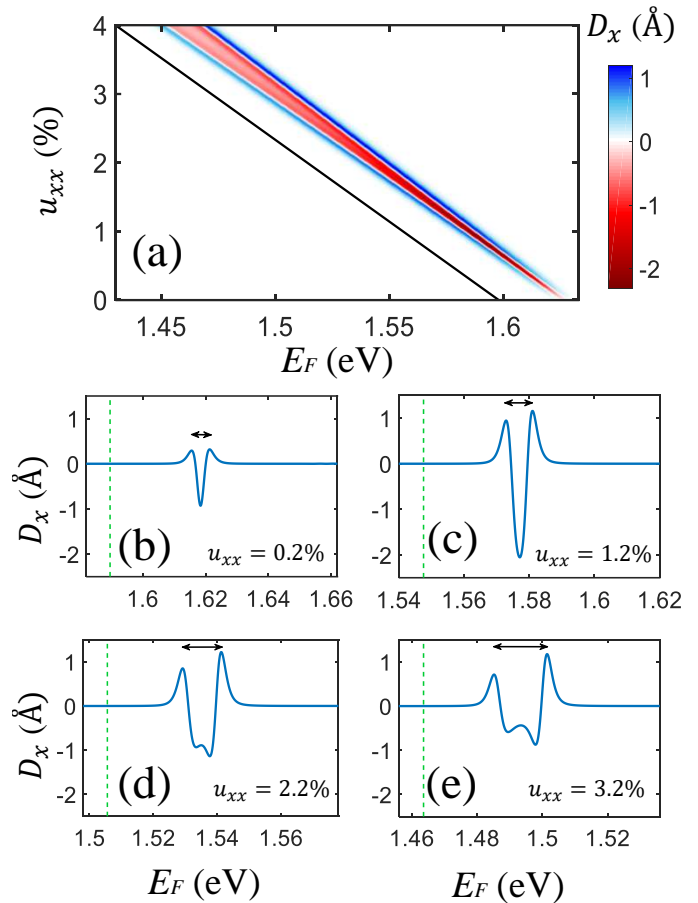


FIG. 3: Evolution of nonlinear Hall signals induced by Berry curvature dipoles in MoSSe under strains and gating. (a) Strain-gate map of Berry dipole D_x in electron-doped MoSSe. Black solid line indicates location of conduction band minimum(CBM). Note that the energy offsets in CBM upon increasing u_{xx} is due to on-site energy corrections induced by strains (see Appendix C). (b)-(e) Gate-dependence of D_x with $u_{xx} = 0.2\%, 1.2\%, 2.2\%, 3.2\%$. Green dashed lines correspond to locations of CBM in each case. The black double arrows indicate the energy separation between anti-crossings associated with the left-movers and the right-movers near the K -valley.

As discussed in subsection B, under a uniaxial strain as strong as $u_{xx} = 4\%$, band anti-crossings associated with the left-movers and right-movers are unambiguously separated in energy. As the Berry curvature hot spots are accessed successively, the sign change in the Berry curvature hot spots are signified by the peak-to-dip/dip-to-peak behaviors in the D_x - E_F curve(Fig.2c).

Notably, the two dips in D_x originate from the left-movers in the upper band and the right-movers in the lower band respectively, with both their band velocities and Berry curvatures being opposite to each other. As a result, their contributions to D_x are additive(Eq.4). Upon decreasing the uniaxial strain, the two dips start to merge with each other, which enhances the total Berry curvature dipole and reaches a maximum $D_x \sim 2\text{\AA}$ for

$u_{xx} \sim 1\%$ as shown in Fig.3a. By further decreasing u_{xx} , while the total D_x would ultimately vanish in the zero strain limit, the additive contributions from merging the two dips in D_x remain strong for weak finite strains. In particular, the magnitude of total D_x is still of the order $\sim 1\text{\AA}$ under $u_{xx} \sim 0.2\%$ where the merging between two dips happens(Fig.3b).

It is also worth noting that the special evolutionary behavior of $D_x - E_F$ curves under strains, particularly the merging effect between the two dips upon decreasing the uniaxial strain, provides yet another unique signature for the gate-tunable nonlinear Hall effect in strained MoSSe.

D. Potential gate-tunable high-frequency rectifiers based on strained polar TMDs

In this section, we discuss how the highly tunable NHE in strained polar TMDs provides a potential scheme for switchable high-frequency rectifiers.

In the past decade, rapid developments of wireless technologies have surged an increasing demand for portable micro-sized devices that can harvest the energy of ambient electromagnetic(EM) radiations. At the heart of these energy harvesters lies the physical process known as rectification, the conversion of oscillating EM fields into DC currents.

While conventional rectifiers based on semiconductor diodes have found a wide range of industrial applications, a fundamental limitation exists for their operating frequencies[37, 38]. In particular, for a preferred current direction to be effectively selected, the diode transition time(*i.e.*, the time scale for a $p - n$ junction to enter a complete open circuit state upon reversing the bias) must be much shorter than the period of EM waves. The typical diode transition time on nanosecond scale sets the maximum frequency limit to lie within the gigahertz range, and the vast amount of energy stored in terahertz and far-infrared radiations, which have natural sources such as thermal radiations, can hardly be harvested with existing rectifiers.

To bypass the frequency threshold, an alternative scheme based on the intrinsic nonlinear property of homogeneous materials was proposed recently[7]. Notably, regardless of the frequency of the applied or ambient AC fields, second-order nonlinearity generically results in a DC response. Thus, the nonlinear Hall effect provides a possible means to build high-frequency rectifiers that can harvest energy of radiations in terahertz and far-infrared regime. In particular, the strained polar TMDs studied in this work can serve as a potential electrically switchable high-frequency rectifier, which controls both the amplitude and direction of rectified currents simply by electric gates.

With the same set-up in Fig.2(d), apart from the second-harmonic component discussed previously, the nonlinear Hall current \mathbf{J}_{NH} generated by an AC electric field $\mathbf{E}_\omega(t) = \text{Re}\{\mathcal{E}_x e^{i\omega t}\}\hat{x}$ is partially rectified due to

the second-order nonlinearity in \mathcal{E}_x , with the DC current component given by[5]:

$$j_y^0 = -\frac{e^3\tau|\mathcal{E}_x|^2}{2(1+i\omega\tau)}D_x. \quad (6)$$

It is clear from Eq.6 that via a moderate gate voltage, the amplitude and direction of the rectified current j_y^0 can be regulated in a similar manner as the $D_x - E_F$ curve in Fig.2(c). This provides an easy way for charge regulation, which is indispensable for real electronic devices. Thus, strained polar TMDs can be used to build a NHE-based high-frequency rectifier which integrates the generation and regulation of charging DC currents within a single device.

III. DISCUSSION

Here, we discuss several important points on nonlinear Hall effects(NHEs) in strained polar TMDs.

First of all, we point out that while strong spin-orbit interactions are known to exist in TMD materials for years[17, 27], the effect of SOCs has been completely ignored in all previous studies on nonlinear Hall physics in strained 2H-TMDs[5, 11]. In this work, we point out for the first time that SOCs can significantly change the nonlinear Hall physics in 2H-TMDs.

Particularly, in usual strained 2H-TMDs where Ω_{spin} is absent, the optimal value of D_x due to Ω_{orb} can only be of order $\sim 0.01\text{\AA}$ under a rather strong uniaxial strain $u_{xx} = 2\%$ [5, 11]. In sharp contrast, due to Ω_{spin} induced by SOCs, strong Berry dipole of order $\sim 1\text{\AA}$ emerges under a weak uniaxial strain $\sim 0.2\%$ (Fig.3).

Moreover, the sign of D_x for electron(hole)-doped samples cannot change due to the fact that the sign of Ω_{orb} is fixed in both conduction and valence bands[5, 11]. On the other hand, as we show explicitly in Fig.3, the nonlinear Hall current becomes highly tunable by gating and strain due to the special property of Ω_{spin} induced by SOCs. Thus, our work demonstrates that SOCs change the nonlinear Hall physics in TMDs in a qualitative way. Also, as the Berry dipole due to Ω_{orb} never changes sign, the sign-changing nonlinear Hall current in strained polar TMDs provides a distinctive electrical signature for the recently discovered Berry curvature Ω_{spin} derived from spin degrees of freedom.

It is important to note that that NHEs in strained polar TMDs generally have a much stronger gate-dependence than $1T_d$ -WTe₂. Strong gate-dependence of NHEs not only provides a practical way to realize gate-tunable Hall devices, but also serves as a distinctive signature of the nontrivial Berry phase origin. In particular, a gate-sensitive nonlinear Hall signal due to Berry curvature dipoles can distinguish itself from trivial mechanisms, such as ratchet effects[5, 14, 16], that are much less sensitive to gating.

In the recent experiment on bilayer $1T'$ -WTe₂, the sign of the Berry curvature dipole D_x is generally fixed in

the neighborhood of the charge neutrality point near the band edges[13]. To switch the sign of D_x , one generally needs to gate the Fermi level to at least 50 – 100 meVs away from the band edges, which requires a rather strong gating field. Furthermore, without a dual-gate set-up, such a strong gating field inevitably introduces out-of-plane displacement fields that cause complications in band structures as well as Berry curvature effects[13]. To unambiguously identify the Berry phase origin of nonlinear Hall effects in 1T_d-WTe₂, a dual-gate set-up is necessary to control the carrier density and the displacement field independently.

In contrast, the Berry curvature dipole in strained polar TMDs can switch its sign dramatically within a narrow Fermi level range $\Delta E_F \sim 10 - 20$ meVs. This range can be easily achieved by a moderate gating, which has been accessed in previous gating experiments on normal 2H-TMDs[39]. Moreover, the strong gate-dependence of D_x in strained polar TMDs occur for Fermi level ~ 20 meV measured from the conduction band edge. This corresponds to a relatively low carrier density regime ($n_{2D} \sim 1 \times 10^{12} \text{cm}^{-2}$), which has also been readily accessed by weak gating[39, 40] without introducing significant displacement field. Thus, a dual-gate set-up is not necessary for detecting the gate-dependence of D_x in strained polar TMDs, and we expect the gate-tunable NHEs in strained polar TMDs to be much more easily observed experimentally comparing to 1T_d-WTe₂.

Besides, the large magnitude and strong gate-tunability of Berry curvature dipole predicted in this work originates from the intrinsic band anti-crossings caused by Ising and Rashba SOCs in moly-based polar TMDs. It does not require any further experimental design apart from strains. To demonstrate the generality of our prediction, we present the gate-dependence of nonlinear Hall signals in another moly-based polar TMD MoSeTe in Appendix E. Same qualitative features in Fig.3 are found in the $D_x - E_F$ curve in strained MoSeTe.

Also, as long as the C_3 -symmetry is broken, details of the strain configuration do not affect our prediction qualitatively. We further point out that for any strain configuration satisfying $u_{xy} = 0$ and $u_{xx} \neq u_{yy}$, the in-plane mirror symmetry $x \mapsto -x$ is preserved in strained MoSSe, with its point group being identical to bilayer/multilayer 1T_d-WTe₂[10, 13]. Thus, the Berry curvature dipole has only a nonzero x -component D_x , which is perpendicular to the mirror plane. In this case, nonlinear Hall effects can be observed as long as the applied electric field deviates from the mirror-invariant y -axis, as demonstrated in the recent experiment on multilayer 1T_d-WTe₂ by Kang et al.[14].

In addition, it is shown previously that Ω_{spin} also arises in tungsten(W)-based TMDs[22]. However, due to the absence of band anti-crossings driven by SOCs in W-based materials, the Berry curvature has a much less non-uniform profile as compared to moly-based case, and the nonlinear Hall effect in W-based polar TMDs is much weaker. Detailed discussions on W-based polar TMDs

are presented in Appendix E.

We note parenthetically that, while a few recent works pointed out possible extrinsic contributions to nonlinear Hall effects due to disorder scattering[41–44], it was suggested that the total nonlinear Hall conductivity remains proportional to the Berry curvature dipole in general[42, 43]. In particular, the recent experiment on bilayer 1T'-WTe₂ unambiguously demonstrated that the sign of the total nonlinear Hall current is almost strictly controlled by the Berry curvature dipole[13]. Thus, we believe the qualitative features of NHEs in polar TMDs predicted in this work will not be affected by extrinsic effects.

Last but not least, for p -type polar TMDs, the effect of Ω_{spin} is almost negligible near the K -points due to the strong Ising SOC ~ 100 meVs in the valence band[26], and the total Berry curvature is dominated by the conventional Ω_{orb} [22]. Thus, for hole-doped polar TMDs, one expects the Berry curvature dipole to be very weak, similar to the case in conventional 2H-TMDs as studied in previous works[5, 11].

Acknowledgement

The authors thank Kaifei Kang and K. F. Mak for illuminating discussions. KTL acknowledges the support of Croucher Foundation, Dr. Tai-chin Lo Foundation and HKRGC through C6026-16W, 16309718, 16307117 and 16324216.

Appendix A: Effective Hamiltonian for strained MoSSe

Here, we derive the effective Hamiltonian near the conduction band minimum for MoSSe by group theory. In the absence of strain, the electronic bands near the conduction band minimum at K -points are dominated by the d_{z^2} -orbitals, with spin degrees of freedom. As we mentioned in the main text, the symmetry group of MoSSe is given by the product group: $C_{3v} \otimes \mathcal{T}$, with the following generators: (i) three-fold rotation (\hat{C}_3), (ii) mirror reflection (\hat{M}_x) and time-reversal \mathcal{T} . The valley index, momentum and spin transform under these generators as follows:

$$\hat{C}_3 : \epsilon \mapsto \epsilon, k_{\pm} \mapsto e^{\pm i2\pi/3} k_{\pm}, \quad (\text{A-1})$$

$$\sigma_{\pm} \mapsto e^{\pm i2\pi/3} \sigma_{\pm}, \sigma_z \mapsto \sigma_z.$$

$$\hat{M}_x : \epsilon \mapsto -\epsilon, k_+ \leftrightarrow -k_-, \sigma_+ \mapsto \sigma_-, \sigma_z \mapsto -\sigma_z.$$

$$\mathcal{T} : \epsilon \mapsto -\epsilon, k_+ \mapsto -k_-, \sigma_+ \mapsto -\sigma_-, \sigma_z \mapsto -\sigma_z.$$

where $\epsilon = \pm$ is the valley index, $k_{\pm} = k_x \pm ik_y$, $\sigma_{\pm} = \sigma_x \pm i\sigma_y$. The unstrained Hamiltonian $H_0(\mathbf{k})$ that are invariant under the transformations in (A-1) has the form (up to second order in \mathbf{k}):

$$H_0(\mathbf{k} + \epsilon\mathbf{K}) = \xi_{\mathbf{k}}\sigma_0 + \epsilon\beta_{so}(\mathbf{k})\sigma_z + \alpha_{so}(k_y\sigma_x - k_x\sigma_y). \quad (\text{A-2})$$

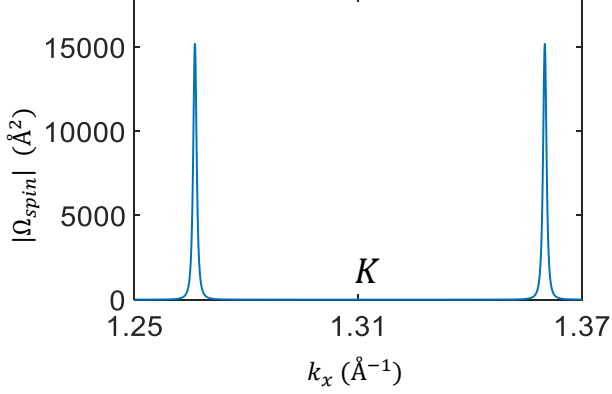


FIG. A-1: Magnitude of Berry curvature generated by Ising and Rashba spin-orbit couplings near K -point of unstrained MoSSe. The coordinate of K -point is given by $\mathbf{K} = (4\pi/3a, 0) \approx (1.313, 0)$ with $a = 3.19\text{\AA}$. Given the effective parameters in Table II, the values of Ω_{orb} are calculated based on Eq.1-2 of the main text. Evidently, huge Ω_{spin} arise in the neighborhood of band-anticrossing points k_0 , with its magnitude generally far greater than 100\AA^2 .

Here $\xi_{\mathbf{k}} = \frac{k^2}{2m^*} - \mu$ is the usual kinetic term, $\beta_{so}(\mathbf{k}) = \beta_0 + \beta_1 k^2$ is the Ising SOC term with $\beta_0\beta_1 < 0$, α_{so} is the strength of Rashba SOC. As we discussed in the main text, in the absence of Rashba SOC, the spin subbands cross each other at $k_0 = \pm\sqrt{\beta_0/\beta_1}$. By turning on the Rashba SOC, nontrivial Berry curvatures arise near the K -point as shown in Fig.A-1, with their magnitude being huge in the neighborhood of k_0 .

Next, we consider corrections terms due to strain. According to Refs.[36], general strain effects in two-dimensional crystalline solids are mathematically described by a displacement field $\mathbf{u}(x, y)$ due to distortions in atomic sites in the strained lattice. In particular, physical effects of strains are described by the gradients of $\mathbf{u}(x, y)$: $\partial_i u_j$, ($i, j = x, y$), which form a second-rank tensor. The four independent components of $\partial_i u_j$ can be classified according to the irreducible representations of C_{3v} : (i) the trace scalar $\partial_x u_x + \partial_y u_y$, which forms the trivial (A_1) representation of C_{3v} ; (ii) the curl (rotation) of \mathbf{u} : $\vec{\omega}_{ij} = \partial_i u_j - \partial_j u_i$ that forms the A_2 -representation of C_{3v} . It describes a rotation of the system about the principal z -axis under strain, which can always be taken away by redefining the coordinates; (iii) the symmetric traceless tensor: $\vec{\epsilon}_{ij} = \frac{1}{2}[\partial_i u_j + \partial_j u_i - (\nabla \cdot \mathbf{u})\delta_{ij}]$, which is characterized by a doublet $\{\partial_x u_y + \partial_y u_x, u_{xx} - u_{yy}\}$ that forms the two-dimensional E -representation of C_{3v} .

To get rid of the redundant rotational part $\vec{\omega}$, the symmetric strain-field tensor $\vec{\mathbf{u}}_{ij} = \frac{1}{2}(\partial_i u_j + \partial_j u_i)$ is introduced such that strain effects are essentially captured by the independent components of $\vec{\mathbf{u}}$. Explicitly, under a group element \hat{g} , the trace $\partial_x u_x + \partial_y u_y \equiv u_{xx} + u_{yy}$ remains invariant, while the doublet $\{\partial_x u_y + \partial_y u_x, u_{xx} -$

$u_{yy}\} \equiv \{2u_{xy}, u_{xx} - u_{yy}\} \equiv \{u_1, u_2\}$ transforms as a polar vector:

$$\hat{g} : \{u_1, u_2\} \mapsto \{u_1, u_2\}[D^{(E)}(\hat{g})]^T. \quad (\text{A-3})$$

where $D^{(E)}(\hat{g})$ denotes the representation matrix for \hat{g} in spatial coordinates: $D_{ij}^{(E)}(\hat{g}) = \mathbf{e}_i \cdot \hat{g} \mathbf{e}_j$, ($i, j = x, y$). Particularly, for the generators \hat{C}_{3z}, \hat{M}_x , the representation matrices are:

$$D^{(E)}(\hat{C}_{3z}) = \begin{pmatrix} -\frac{1}{2} & -\frac{\sqrt{3}}{2} \\ \frac{\sqrt{3}}{2} & \frac{1}{2} \end{pmatrix}, \quad (\text{A-4})$$

$$D^{(E)}(\hat{M}_x) = \begin{pmatrix} -1 & 0 \\ 0 & 1 \end{pmatrix}.$$

To sum up the symmetry properties of the physical quantities mentioned above, the irreducible representations of the valley index, momentum, spin and strain-tensor components are presented in Table I.

In the presence of the strain-field tensor $\vec{\mathbf{u}}$, the underlying point group symmetries in C_{3v} is manifested by the following equivalence: Given any $\hat{g} \in C_{3v}$, after being transformed by \hat{g} , the system with strain $\vec{\mathbf{u}}$ is identical to the system with transformed strain $\vec{\mathbf{u}}' = \hat{g} \vec{\mathbf{u}}$. Here, components of $\vec{\mathbf{u}}'$ and $\vec{\mathbf{u}}$ are related by: $u'_0 = u_0, \{u'_1, u'_2\} = \{u_1, u_2\}[D^{(E)}(\hat{g})]^T$.

Formally, this can be expressed as:

$$\hat{g} \hat{H}(\vec{\mathbf{u}}) \hat{g}^{-1} = \hat{H}(\hat{g} \vec{\mathbf{u}}). \quad (\text{A-5})$$

where $\hat{H}(\vec{\mathbf{u}})$ is the total Hamiltonian under strain $\vec{\mathbf{u}}$. Note that the symmetry relation above is simply a generalization of the symmetry property of unstrained system with $\vec{\mathbf{u}} = \mathbf{0}$. Particularly, Eq.A-5 implies that the momentum-space Hamiltonian $H(\mathbf{k})$ satisfies:

$$U^\dagger(\hat{g})H(\hat{g}\mathbf{k}, \hat{g}\vec{\mathbf{u}})U(\hat{g}) = H(\mathbf{k}, \vec{\mathbf{u}}). \quad (\text{A-6})$$

where $U(\hat{g})$ denotes the matrix for group operator \hat{g} under the spin basis: $U_{\sigma\sigma'}(\hat{g}) = \langle \sigma | \hat{g} | \sigma' \rangle$, with $\sigma, \sigma' = \uparrow, \downarrow$. Accordingly, up to first order in \mathbf{k} , strain effects on the spin-independent terms are described by:

$$H_{strain}(\mathbf{k} + \epsilon\mathbf{K}) = [\gamma u_0 + \epsilon\delta(k_y u_1 - k_x u_2)]\sigma_0. \quad (\text{A-7})$$

The $\gamma u_0 \sigma_0$ -term describes the on-site energy correction due to strain, which causes an energy offset in the conduction band minimum. The $\epsilon\delta(k_x u_2 - k_y u_1)$ -term results from the correction in the bonding strengths due to modified inter-atomic distances in the strained lattice. This term explicitly breaks the C_3 -symmetry, which is responsible for the nonzero Berry curvature dipole discussed in the main text. The total Hamiltonian is

$$H_{eff} = H_0 + H_{strain}. \quad (\text{A-8})$$

The parameters of the effective Hamiltonian can be obtained by fitting the realistic band structures, which are listed in Table II. Notably, due to $\delta < 0$, the uniaxial

TABLE I: Irreducible representations(IR)s of valley index, momentum, spin, and strain-tensor components in C_{3v} and parity under time-reversal \mathcal{T} .

Basis functions	IR	\mathcal{T}
ϵ	A_2	-
$1, k_x^2 + k_y^2$	A_1	+
$\{k_x, k_y\}$	E	-
σ_0	A_1	+
σ_z	A_2	-
$\{\sigma_x, \sigma_y\}$	E	-
u_0	A_1	+
$\{u_1, u_2\}$	E	+

strain with $u_{xx} > 0, u_{yy} = u_{xy} = 0$ causes a shift of the band minimum at $+K(-K)$ to the left(right), as being consistent with our discussions in the main text. Also, due to $\gamma < 0$, the energy offset due to strain is negative for $u_{xx} > 0$. By increasing u_{xx} , the conduction band minimum gets lower in energy, which is also consistent with the results in Fig.4 of the main text.

TABLE II: Parameters for the effective Hamiltonian H_{eff} .

m^*/m_e	$\alpha_{so}/a(\text{meV})$	$\beta_0(\text{meV})$	$\beta_1/a^2(\text{meV})$
0.5	0.3	-1.5	67
$\gamma(\text{eV})$	$\delta/a(\text{eV})$	$a(\text{\AA})$	
-4.2	-1.5	3.19	

Appendix B: Tight-binding Hamiltonian

The tight-binding(TB) Hamiltonian for MoS₂ and MoSSe takes the same form, with the only difference that the Rashba spin-orbit coupling(SOC) for pristine MoS₂ is zero. In generic monolayer transition-metal dichalcogenides, the conduction and valence band edges are dominated by the $d_{z^2}, d_{xy}, d_{x^2-y^2}$ orbitals from the transition-metal atoms[26]. In the spinful Bloch basis of the d -orbitals: $\{|\mathbf{k}, d_{z^2}\rangle, |\mathbf{k}, d_{xy}\rangle, |\mathbf{k}, d_{x^2-y^2}\rangle\}$, the unstrained tight-binding Hamiltonian for polar TMD up to nearest-neighbor hopping is written as

$$H_{\text{TB}}^0(\mathbf{k}) = H_{\text{NN}}(\mathbf{k}) \otimes \sigma_0 + \frac{1}{2}\lambda L_z \otimes \sigma_z \quad (\text{B-1})$$

$$+ H_R(\mathbf{k}) + H_I^c(\mathbf{k}).$$

Next, we present the Ising and Rashba SOC in the tight-binding model. Note that the Ising SOC in the

The first term $H_{\text{NN}}(\mathbf{k})$ represents the spin-independent terms, the second term refers to the atomic spin-orbit coupling. $H_R(\mathbf{k})$ and $H_I^c(\mathbf{k})$ describe the Rashba SOC and the Ising SOC near the conduction band edges. The first two terms are given by[26]:

$$H_{\text{NN}}(\mathbf{k}) = \begin{pmatrix} V_0 & V_1 & V_2 \\ V_1^* & V_{11} & V_{12} \\ V_2^* & V_{12}^* & V_{22} \end{pmatrix} - \mu I_{3 \times 3}, \quad (\text{B-2})$$

$$L_z = \begin{pmatrix} 0 & 0 & 0 \\ 0 & 0 & -2i \\ 0 & 2i & 0 \end{pmatrix}$$

Here, μ denotes the chemical potential, and L_z is the z -component of the orbital angular momentum. Defining $(\alpha, \beta) = \left(\frac{1}{2}k_x a, \frac{\sqrt{3}}{2}k_y a\right)$, $V_0, V_1, V_2, V_{11}, V_{12}$ and V_{22} are expressed as:

$$V_0 = \epsilon_1 + 2t_0(2\cos\alpha\cos\beta + \cos 2\alpha), \quad (\text{B-3})$$

$$\text{Re}[V_1] = -2\sqrt{3}t_2\sin\alpha\sin\beta, \quad (\text{B-4})$$

$$\text{Im}[V_1] = 2t_1\sin\alpha(2\cos\alpha + \cos\beta), \quad (\text{B-5})$$

$$\text{Re}[V_2] = 2t_2(\cos 2\alpha - \cos\alpha\cos\beta), \quad (\text{B-6})$$

$$\text{Im}[V_2] = 2\sqrt{3}t_1\cos\alpha\sin\beta, \quad (\text{B-7})$$

$$V_{11} = \epsilon_2 + (t_{11} + 3t_{22})\cos\alpha\cos\beta + 2t_{11}\cos 2\alpha, \quad (\text{B-8})$$

$$\text{Re}[V_{12}] = \sqrt{3}(t_{22} - t_{11})\sin\alpha\sin\beta, \quad (\text{B-9})$$

$$\text{Im}[V_{12}] = 4t_{12}\sin\alpha(\cos\alpha - \cos\beta), \quad (\text{B-10})$$

and

$$V_{22} = \epsilon_2 + (3t_{11} + t_{22})\cos\alpha\cos\beta + 2t_{22}\cos 2\alpha. \quad (\text{B-11})$$

The parameters for the NN tight-binding model are adapted from Refs.[26] and listed in Table III.

valence bands are readily described by $H_{\text{NN}}(\mathbf{k})$ together with the atomic spin-orbit coupling term. The Ising SOC

TABLE III: Parameters for $H_{\text{NN}}(\mathbf{k})$ for monolayer MoS₂ and MoSe₂ adapted from Refs.[26]. All energy parameters set in units of eV .

	$a(\text{\AA})$	ϵ_1	ϵ_2	t_0	t_1	t_2	t_{11}	t_{12}	t_{22}	λ
MoS ₂	3.190	1.046	2.104	-0.184	0.401	0.507	0.218	0.338	0.057	-0.073
MoSe ₂	3.326	0.919	2.065	-0.188	0.317	0.456	0.211	0.290	0.130	-0.091

in the conduction bands $H_I^c(\mathbf{k})$ takes the form:

$$H_I^c(\mathbf{k}) = \begin{pmatrix} \beta(\mathbf{k}) & 0 & 0 \\ 0 & 0 & 0 \\ 0 & 0 & 0 \end{pmatrix} \otimes \sigma_z. \quad (\text{B-12})$$

where

$$\beta(\mathbf{k}) = -\frac{2\beta_{so}^c}{3\sqrt{3}}[\sin(2\alpha) - 2\sin(\alpha)\cos(\beta)]. \quad (\text{B-13})$$

with $\beta_{so}^c = -1.5$ meV. The Rashba SOC $H_R(\mathbf{k})$ is written as:

$$H_R(\mathbf{k}) = \begin{pmatrix} 2\alpha_0 & 0 & 0 \\ 0 & 0 & 0 \\ 0 & 0 & 0 \end{pmatrix} \otimes (f_x(\mathbf{k})\sigma_y - f_y(\mathbf{k})\sigma_x). \quad (\text{B-14})$$

where α_0 denotes the tight-binding Rashba parameter for d_{z^2} -orbitals. In our tight-binding calculations, we set $\alpha_0 = 0.2$ meV for MoSSe. We note that α_0 is related to the effective Rashba strength α_{so} in the effective model by: $\alpha_{so} = \frac{3}{2}\alpha_0 a$, where a is the lattice constant. The Rashba SOC for $\{d_{xy}, d_{x^2-y^2}\}$ orbitals are neglected as we only concern about the conduction band minimum which is dominated by d_{z^2} -orbitals. The functions $f_x(\mathbf{k}), f_y(\mathbf{k})$ are given by:

$$\begin{aligned} f_x(\mathbf{k}) &= \sin(2\alpha) + \sin(\alpha)\cos(\beta) \\ f_y(\mathbf{k}) &= \sqrt{3}\sin(\beta)\cos(\alpha) \end{aligned} \quad (\text{B-15})$$

Appendix C: Symmetry-allowed linear coupling to strain-field

Considering $\{d_{z^2}, d_{xy}, d_{x^2-y^2}\}$ -orbitals, the general form of real-space tight-binding Hamiltonian is given by:

$$\hat{H}(\overleftarrow{\mathbf{u}}) = \sum_{\mathbf{R}, \mathbf{R}'} \sum_{\alpha, \beta} c_{\alpha}^{\dagger}(\mathbf{R}) h_{\alpha, \beta}(\mathbf{R}, \mathbf{R}', \overleftarrow{\mathbf{u}}) c_{\beta}^{\dagger}(\mathbf{R}') \quad (\text{C-1})$$

where \mathbf{R}, \mathbf{R}' label the lattice sites, and α, β are the orbital/spin indices. Based on the general relation defined in Eq.A-5 of Section I, the matrix connecting a general pair of lattice sites \mathbf{R}, \mathbf{R}' satisfy the following relation:

$$\hat{h}(\hat{g}\mathbf{R}, \hat{g}\mathbf{R}', \overleftarrow{\mathbf{u}}) = U(\hat{g})\hat{h}(\mathbf{R}, \mathbf{R}', \hat{g}^{-1}\overleftarrow{\mathbf{u}})U^{\dagger}(\hat{g}). \quad (\text{C-2})$$

Note that Eq.C-2 is simply a generalization of the symmetry relations for unstrained case as studied in

Refs.[26], should we enforce that under \hat{g} the strain-field tensor transforms inversely to $\overleftarrow{\mathbf{u}}' = \hat{g}^{-1}\overleftarrow{\mathbf{u}}$, with $u'_0 = u_0, \{u'_1, u'_2\} = \{u_1, u_2\}[D^{(E)}(\hat{g}^{-1})]^T$.

Under weak applied strains considered in this work, it is reasonable to assume that corrections due to strain are essentially given by linear-order coupling to the strain-field components in $\overleftarrow{\mathbf{u}}$. In particular, the on-site terms are invariant under the generalized transformation in Eq.C-2, which take the following form:

$$\begin{aligned} \hat{h}_0(\overleftarrow{\mathbf{u}}) &= (u_{xx} + u_{yy}) \begin{pmatrix} E_0^S & 0 & 0 \\ 0 & E_2^S & 0 \\ 0 & 0 & E_2^S \end{pmatrix} \\ &+ 2u_{xy} \begin{pmatrix} 0 & h_1^S & 0 \\ h_1^S & 0 & h_2^S \\ 0 & h_2^S & 0 \end{pmatrix} \\ &+ (u_{xx} - u_{yy}) \begin{pmatrix} 0 & 0 & h_1^S \\ 0 & h_2^S & 0 \\ h_1^S & 0 & -h_2^S \end{pmatrix}. \end{aligned} \quad (\text{C-3})$$

Next, let us consider nearest-neighbor terms. According to Eq.C-2, given the hopping term $\hat{h}(\boldsymbol{\delta}, \overleftarrow{\mathbf{u}})$ along a certain bonding vector $\boldsymbol{\delta} = \mathbf{R} - \mathbf{R}'$, the hopping Hamiltonian along the transformed bonding vector $\boldsymbol{\delta}' = \hat{g}\boldsymbol{\delta}$ can be explicitly given by:

$$\hat{h}(\boldsymbol{\delta}', \overleftarrow{\mathbf{u}}) = U(\hat{g})\hat{h}(\boldsymbol{\delta}, \hat{g}^{-1}\overleftarrow{\mathbf{u}})U^{\dagger}(\hat{g}) \quad (\text{C-4})$$

Thus, with the knowledge of the hopping Hamiltonian $\hat{h}(\boldsymbol{\delta}, \overleftarrow{\mathbf{u}})$ along $\boldsymbol{\delta}$, hopping terms along all bonding vectors $\boldsymbol{\delta}' = \hat{g}\boldsymbol{\delta}$ can be obtained by acting \hat{g} 's on $\hat{h}(\boldsymbol{\delta}, \overleftarrow{\mathbf{u}})$. The symmetry allowed form for $\hat{h}(\boldsymbol{\delta}_1 \equiv a\hat{x}, \overleftarrow{\mathbf{u}})$ is given by[36]:

$$\begin{aligned} \hat{h}(\boldsymbol{\delta}_1, \overleftarrow{\mathbf{u}}) &= u_0\hat{P}^{(A_1)} + u_1\hat{N}^{(E)} + u_2\hat{P}^{(E)} \\ &= (u_{xx} + u_{yy}) \begin{pmatrix} P_{00}^{(A_1)} & P_{01}^{(A_1)} & P_{02}^{(A_1)} \\ -P_{01}^{(A_1)} & P_{11}^{(A_1)} & P_{12}^{(A_1)} \\ P_{02}^{(A_1)} & -P_{12}^{(A_1)} & P_{22}^{(A_1)} \end{pmatrix} \\ &+ (u_{xx} - u_{yy}) \begin{pmatrix} P_{00}^{(E)} & P_{01}^{(E)} & P_{02}^{(E)} \\ -P_{01}^{(E)} & P_{11}^{(E)} & P_{12}^{(E)} \\ P_{02}^{(E)} & -P_{12}^{(E)} & P_{22}^{(E)} \end{pmatrix} \\ &+ 2u_{xy} \begin{pmatrix} 0 & N_{01}^{(E)} & N_{02}^{(E)} \\ N_{01}^{(E)} & 0 & N_{12}^{(E)} \\ -N_{02}^{(E)} & N_{12}^{(E)} & 0 \end{pmatrix}. \end{aligned} \quad (\text{C-5})$$

The bonds in the direction $\delta' = \hat{C}_{3z}\delta$ are related to the bonds in the direction δ by[36]:

$$\hat{h}(\delta', \overleftarrow{\mathbf{u}}) = U(\hat{C}_{3z})\hat{h}(\delta, \hat{C}_{3z}^{-1}\overleftarrow{\mathbf{u}})U^\dagger(\hat{C}_{3z}) \quad (\text{C-6})$$

where

$$U(\hat{C}_{3z}) = \begin{pmatrix} 1 & 0 & 0 \\ 0 & -\frac{1}{2} & -\frac{\sqrt{3}}{2} \\ 0 & \frac{\sqrt{3}}{2} & -\frac{1}{2} \end{pmatrix} \quad (\text{C-7})$$

And for the transformed strain tensor field $\overleftarrow{\mathbf{u}}' = \hat{C}_{3z}^{-1}\overleftarrow{\mathbf{u}}$,

we have:

$$u'_{xx} - u'_{yy} = -\frac{1}{2}(u_{xx} - u_{yy}) - \frac{\sqrt{3}}{2}(2u_{xy}) \quad (\text{C-8})$$

$$2u'_{xy} = -\frac{1}{2}(2u_{xy}) + \frac{\sqrt{3}}{2}(u_{xx} - u_{yy})$$

in accord with the E -representation of C_{3v} . Now, with the general form of $\hat{h}(\delta_1, \overleftarrow{\mathbf{u}})$ in Eq.C-5, we obtain the hopping terms in $\delta_2 \equiv \hat{C}_{3z}\delta_1$ and $\delta_3 \equiv \hat{C}_{3z}^2\delta_1$ using the relations above, which are given by:

$$\begin{aligned} \hat{h}(\delta_2, \overleftarrow{\mathbf{u}}) = & (u_{xx} + u_{yy}) \begin{pmatrix} P_{00}^{(A1)} & -\frac{1}{2}P_{01}^{(A1)} - \frac{\sqrt{3}}{2}P_{02}^{(A1)} & \frac{\sqrt{3}}{2}P_{01}^{(A1)} - \frac{1}{2}P_{02}^{(A1)} \\ \frac{1}{2}P_{01}^{(A1)} - \frac{\sqrt{3}}{2}P_{02}^{(A1)} & \frac{1}{4}P_{11}^{(A1)} + \frac{3}{4}P_{22}^{(A1)} & P_{12}^{(A1)} + \frac{\sqrt{3}}{4}(P_{22}^{(A1)} - P_{11}^{(A1)}) \\ -\frac{\sqrt{3}}{2}P_{01}^{(A1)} - \frac{1}{2}P_{02}^{(A1)} & -P_{12}^{(A1)} + \frac{\sqrt{3}}{4}(P_{22}^{(A1)} - P_{11}^{(A1)}) & \frac{3}{4}P_{11}^{(A1)} + \frac{1}{4}P_{22}^{(A1)} \end{pmatrix} \\ & + [-\frac{\sqrt{3}}{2}(2u_{xy}) - \frac{1}{2}(u_{xx} - u_{yy})] \begin{pmatrix} P_{00}^{(E)} & -\frac{1}{2}P_{01}^{(E)} - \frac{\sqrt{3}}{2}P_{02}^{(E)} & \frac{\sqrt{3}}{2}P_{01}^{(E)} - \frac{1}{2}P_{02}^{(E)} \\ \frac{1}{2}P_{01}^{(E)} - \frac{\sqrt{3}}{2}P_{02}^{(E)} & \frac{1}{4}P_{11}^{(E)} + \frac{3}{4}P_{22}^{(E)} & P_{12}^{(E)} + \frac{\sqrt{3}}{4}(P_{22}^{(E)} - P_{11}^{(E)}) \\ -\frac{\sqrt{3}}{2}P_{01}^{(E)} - \frac{1}{2}P_{02}^{(E)} & -P_{12}^{(E)} + \frac{\sqrt{3}}{4}(P_{22}^{(E)} - P_{11}^{(E)}) & \frac{3}{4}P_{11}^{(E)} + \frac{1}{4}P_{22}^{(E)} \end{pmatrix} \\ & + [-\frac{1}{2}(2u_{xy}) + \frac{\sqrt{3}}{2}(u_{xx} - u_{yy})] \begin{pmatrix} 0 & -\frac{1}{2}N_{01}^{(E)} - \frac{\sqrt{3}}{2}N_{02}^{(E)} & \frac{\sqrt{3}}{2}N_{01}^{(E)} - \frac{1}{2}N_{02}^{(E)} \\ -\frac{1}{2}N_{01}^{(E)} + \frac{\sqrt{3}}{2}N_{02}^{(E)} & \frac{\sqrt{3}}{2}N_{12}^{(E)} & -\frac{1}{2}N_{12}^{(E)} \\ \frac{\sqrt{3}}{2}N_{01}^{(E)} + \frac{1}{2}N_{02}^{(E)} & -\frac{1}{2}N_{12}^{(E)} & -\frac{\sqrt{3}}{2}N_{12}^{(E)} \end{pmatrix} \end{aligned} \quad (\text{C-9})$$

$$\begin{aligned} \hat{h}(\delta_3, \overleftarrow{\mathbf{u}}) = & (u_{xx} + u_{yy}) \begin{pmatrix} P_{00}^{(A1)} & -\frac{1}{2}P_{01}^{(A1)} + \frac{\sqrt{3}}{2}P_{02}^{(A1)} & -\frac{\sqrt{3}}{2}P_{01}^{(A1)} - \frac{1}{2}P_{02}^{(A1)} \\ \frac{1}{2}P_{01}^{(A1)} + \frac{\sqrt{3}}{2}P_{02}^{(A1)} & \frac{1}{4}P_{11}^{(A1)} + \frac{3}{4}P_{22}^{(A1)} & P_{12}^{(A1)} - \frac{\sqrt{3}}{4}(P_{22}^{(A1)} - P_{11}^{(A1)}) \\ \frac{\sqrt{3}}{2}P_{01}^{(A1)} - \frac{1}{2}P_{02}^{(A1)} & -P_{12}^{(A1)} - \frac{\sqrt{3}}{4}(P_{22}^{(A1)} - P_{11}^{(A1)}) & \frac{3}{4}P_{11}^{(A1)} + \frac{1}{4}P_{22}^{(A1)} \end{pmatrix} \\ & + [\frac{\sqrt{3}}{2}(2u_{xy}) - \frac{1}{2}(u_{xx} - u_{yy})] \begin{pmatrix} P_{00}^{(E)} & -\frac{1}{2}P_{01}^{(E)} + \frac{\sqrt{3}}{2}P_{02}^{(E)} & -\frac{\sqrt{3}}{2}P_{01}^{(E)} - \frac{1}{2}P_{02}^{(E)} \\ \frac{1}{2}P_{01}^{(E)} + \frac{\sqrt{3}}{2}P_{02}^{(E)} & \frac{1}{4}P_{11}^{(E)} + \frac{3}{4}P_{22}^{(E)} & P_{12}^{(E)} - \frac{\sqrt{3}}{4}(P_{22}^{(E)} - P_{11}^{(E)}) \\ \frac{\sqrt{3}}{2}P_{01}^{(E)} - \frac{1}{2}P_{02}^{(E)} & -P_{12}^{(E)} - \frac{\sqrt{3}}{4}(P_{22}^{(E)} - P_{11}^{(E)}) & \frac{3}{4}P_{11}^{(E)} + \frac{1}{4}P_{22}^{(E)} \end{pmatrix} \\ & + [-\frac{1}{2}(2u_{xy}) - \frac{\sqrt{3}}{2}(u_{xx} - u_{yy})] \begin{pmatrix} 0 & -\frac{1}{2}N_{01}^{(E)} + \frac{\sqrt{3}}{2}N_{02}^{(E)} & -\frac{\sqrt{3}}{2}N_{01}^{(E)} - \frac{1}{2}N_{02}^{(E)} \\ -\frac{1}{2}N_{01}^{(E)} - \frac{\sqrt{3}}{2}N_{02}^{(E)} & -\frac{\sqrt{3}}{2}N_{12}^{(E)} & -\frac{1}{2}N_{12}^{(E)} \\ -\frac{\sqrt{3}}{2}N_{01}^{(E)} + \frac{1}{2}N_{02}^{(E)} & -\frac{1}{2}N_{12}^{(E)} & \frac{\sqrt{3}}{2}N_{12}^{(E)} \end{pmatrix} \end{aligned} \quad (\text{C-10})$$

The Hermitian property of H implies that: $h(\delta, \overleftarrow{\mathbf{u}}) = h^\dagger(-\delta, \overleftarrow{\mathbf{u}})$, thus the rest of the hopping terms in $-\delta_i$ ($i = 1, 2, 3$) can simply be obtained by hermitian conjugation. With hopping terms along all bonding vectors above, we Fourier transform the Wannier operators:

$$\hat{c}_\alpha^\dagger(\mathbf{R}) = \frac{1}{\sqrt{N}} \sum_{\mathbf{k}} e^{-i\mathbf{k}\cdot\mathbf{R}} \hat{c}_{\mathbf{k}\alpha}^\dagger \quad (\text{C-11})$$

and the hopping terms in momentum-space become

$$h_1(\mathbf{k}, \overleftarrow{\mathbf{u}}) = \sum_{n=1}^3 e^{-i\mathbf{k}\cdot\delta_n} \hat{h}(\delta_n, \overleftarrow{\mathbf{u}}) + h.c. \quad (\text{C-12})$$

The strained momentum-space Hamiltonian can be ob-

tained as:

$$H_{\text{TB}}^S(\mathbf{k}) = h_0(\overleftarrow{\mathbf{u}}) \otimes \sigma_0 + h_1(\mathbf{k}, \overleftarrow{\mathbf{u}}) \otimes \sigma_0. \quad (\text{C-13})$$

Thus, the total tight-binding Hamiltonian for strained 2H-TMDs is given by:

$$H_{\text{TB}}(\mathbf{k}) = H_{\text{TB}}^0(\mathbf{k}) + H_{\text{TB}}^S(\mathbf{k}). \quad (\text{C-14})$$

The model parameters for $H_{\text{TB}}(\mathbf{k})$ used in calculating Fig.2 & 3 of the main text are presented in Table III(unstrained parameters) and Table IV(strained parameters).

TABLE IV: Strained tight-binding parameters up to nearest-neighbor(NN) hopping terms for monolayer MoS₂ and MoSe₂ adapted from Refs.[36]. All parameters are set in units of eV.

		MoS ₂				MoSe ₂						
On-site	E_0^S	E_2^S	h_1^S	h_2^S	E_0^S	E_2^S	h_1^S	h_2^S				
	-1.021	-1.817	-0.043	-0.370	-1.090	-2.023	0.004	-0.296				
NN	$P_{00}^{(A1)}$	$P_{01}^{(A1)}$	$P_{02}^{(A1)}$	$P_{11}^{(A1)}$	$P_{12}^{(A1)}$	$P_{22}^{(A1)}$	$P_{00}^{(A1)}$	$P_{01}^{(A1)}$	$P_{02}^{(A1)}$	$P_{11}^{(A1)}$	$P_{12}^{(A1)}$	$P_{22}^{(A1)}$
	1.032	-0.285	-0.738	-1.027	0.206	1.544	0.885	-0.236	-0.596	-0.951	0.195	1.333
	$P_{00}^{(E)}$	$P_{01}^{(E)}$	$P_{02}^{(E)}$	$P_{11}^{(E)}$	$P_{12}^{(E)}$	$P_{22}^{(E)}$	$P_{00}^{(E)}$	$P_{01}^{(E)}$	$P_{02}^{(E)}$	$P_{11}^{(E)}$	$P_{12}^{(E)}$	$P_{22}^{(E)}$
	0.376	-0.188	-0.779	-0.910	-0.003	1.337	0.333	-0.126	-0.667	-0.793	0.008	1.108
	$N_{01}^{(E)}$	$N_{02}^{(E)}$	$N_{12}^{(E)}$									
	0.288	0.152	-0.634									
	$N_{01}^{(E)}$	$N_{02}^{(E)}$	$N_{12}^{(E)}$									
	0.255	0.110	-0.565									

Appendix D: Strongly enhanced Berry dipole due to SOC's

In the main text, we mentioned that Ω_{spin} not only enhances the magnitude of total Berry curvature Ω_{tot} but also results in a highly nonuniform momentum-space profile for Ω_{tot} . In this section, we discuss in details how Ω_{spin} leads to Ω_{tot} with very large magnitudes and nonuniform profile, and then explain why these special properties result in strongly enhanced Berry curvature dipole in strained MoSSe.

First of all, we show that, in the regime where large Berry dipoles emerge (Fermi level lying close to the band anti-crossing points), the total Berry curvature Ω_{tot} in the electron bands can be approximately given as an algebraic sum of Ω_{spin} and Ω_{orb} , *i.e.*, $\Omega_{tot} \approx \Omega_{spin} + \Omega_{orb}$.

To demonstrate the relation $\Omega_{tot} \approx \Omega_{spin} + \Omega_{orb}$, we consider $K = (4\pi/3a, 0)$ with the physics near $-K$ followed by time-reversal symmetry. In the Bloch basis of $|d_{c,\uparrow}\rangle, |d_{c,\downarrow}\rangle, |d_{v,\uparrow}\rangle, |d_{v,\downarrow}\rangle$, the four-band Hamiltonian near K can be written as[17, 22]:

$$H_{tot}(\mathbf{k}) = \begin{pmatrix} \frac{\Delta}{2} + (\beta_0 + \beta'_1 k^2) & -i\alpha_{so}(k_x + ik_y) & V_F(k_x - ik_y) & 0 \\ i\alpha_{so}(k_x - ik_y) & \frac{\Delta}{2} - (\beta_0 + \beta'_1 k^2) & 0 & V_F(k_x - ik_y) \\ V_F(k_x + ik_y) & 0 & -\frac{\Delta}{2} + \lambda & 0 \\ 0 & V_F(k_x + ik_y) & 0 & -\frac{\Delta}{2} - \lambda \end{pmatrix}. \quad (D-1)$$

Here, $|d_{c,\alpha}\rangle \equiv |d_{z^2}, \alpha\rangle$ denotes the predominant $|d_{z^2}\rangle$ -orbital with spin $\alpha = \uparrow, \downarrow$ at the conduction band edge at K , and $|d_{v,\alpha}\rangle \equiv |d_{x^2-y^2} + id_{xy}, \alpha\rangle$ denotes the predominant $|d_{x^2-y^2} + id_{xy}\rangle$ -orbital with spin $\alpha = \uparrow, \downarrow$ at the valence band edge at K . $V_F = 3.5eV \cdot \text{\AA}$ is the effective inter-orbital hopping parameter, $\Delta = 1.66eV$ is the band gap at K , and $\lambda \approx 50$ meVs describes the Ising SOC strength in the valence band. The parameters β_0, α_{so} are defined in the same way as in the main text. However, β'_1

is not to be identified with β_1 in Eq.1-2 of the main text. The relation between β_1 and the parameters $\beta'_1, V_F, \Delta, \lambda$ will become clear in the following discussions.

Without loss of generality, we demonstrate the case of the lower SOC-split conduction band (band index: $n = c, -$). The analysis for the upper SOC-split conduction band ($n = c, +$) is similar. For any momentum \mathbf{k} displaced from K , the *exact* form of total Berry curvature in the lower conduction band is given by:

$$\begin{aligned}
\Omega_{c,-}^{tot}(\mathbf{k}) &= \Omega_{c,-}^{inter}(\mathbf{k}) + \Omega_{c,-}^{intra}(\mathbf{k}), \\
\Omega_{c,-}^{inter}(\mathbf{k}) &= i \sum_{m=\pm} \frac{\langle c, -, \mathbf{k} | \hat{v}_x | v, m, \mathbf{k} \rangle \langle v, m, \mathbf{k} | \hat{v}_y | c, -, \mathbf{k} \rangle - c.c.}{(E_{c,-}(\mathbf{k}) - E_{v,m}(\mathbf{k}))^2}, \\
\Omega_{c,-}^{intra}(\mathbf{k}) &= i \frac{\langle c, -, \mathbf{k} | \hat{v}_x | c, +, \mathbf{k} \rangle \langle c, +, \mathbf{k} | \hat{v}_y | c, -, \mathbf{k} \rangle - c.c.}{(E_{c,-}(\mathbf{k}) - E_{c,+}(\mathbf{k}))^2}.
\end{aligned} \tag{D-2}$$

Here, $n = c/v, +/-$ is the band index for Bloch eigenstate $|n, \mathbf{k}\rangle$ of $H_{tot}(\mathbf{k})$, associated with band energy $E_n(\mathbf{k})$. $+/-$ labels the upper/lower SOC-split bands, and c/v labels the conduction/valence band. $\hat{v}_i \equiv \partial H_{tot} / \partial k_i$, with $i = x, y$, is the velocity operator in the i -direction.

As shown in Ref.[22], at exactly the K -point ($\mathbf{k} = \mathbf{0}$), the Ω^{inter} -term in the second line of Eq.D-2 arises from interband coupling between conduction and valence bands. It reduces to the orbital-type Berry curvature Ω_{orb} . The Ω^{intra} -term in the third line of Eq.D-2 arises from intra-band coupling between the two conduction bands which are split by SOCs. It reduces to the spin-type Berry curvature Ω_{spin} at exactly the K -point. Thus, $\Omega_{tot} = \Omega_{spin} + \Omega_{orb}$ holds strictly at the K -point. It was also pointed out in Ref.[22] that, based on the symmetry property of Berry curvature around C_3 -invariant K -points, $\Omega_{tot} \approx \Omega_{spin} + \Omega_{orb}$ holds in the close vicinity of K .

Now, we show that throughout the Fermi level regime considered in this work, $\Omega^{intra} \approx \Omega_{spin}$ and $\Omega^{inter} \approx \Omega_{orb}$ holds. As a result, we have $\Omega_{tot} \approx \Omega_{spin} + \Omega_{orb}$. To see why $\Omega^{intra} \approx \Omega_{spin}$, we note that at a finite momentum \mathbf{k} , the weight of the $|d_v\rangle \equiv |d_{x^2-y^2} + id_{xy}\rangle$ -states in the eigenstates $|c, \pm, \mathbf{k}\rangle$ of conduction bands is of the order $w_v \sim V_F^2 k^2 / \Delta^2$ according to perturbation theory. As the relevant Fermi level ranges from 0 – 30 meV measured from the conduction band minimum, the relevant momentum range covers $0 \text{ \AA}^{-1} < k < 0.06 \text{ \AA}^{-1}$ measured from $K = 1.31 \text{ \AA}^{-1}$ (Fig.A-1). With $V_F = 3.5eV \cdot \text{ \AA}$ and $\Delta = 1.66eV$, the weight of $|d_{x^2-y^2} + id_{xy}\rangle$ -state is $w_v < 2\%$ throughout this range. This suggests that in all ranges of Fermi level studied in this work, electronic states in the conduction band are strongly dominated by the $|d_c\rangle \equiv |d_{z^2}\rangle$ -orbitals.

The negligible contribution from $|d_{x^2-y^2} + id_{xy}\rangle$ -states in the electronic wavefunctions allows us to construct an effective two-band Hamiltonian $H_{eff}(\mathbf{k})$ formed by $\{|d_{z^2}, \uparrow\rangle, |d_{z^2}, \downarrow\rangle\}$ -states for conduction band electrons within the range $0 \text{ \AA}^{-1} < k < 0.06 \text{ \AA}^{-1}$, such that the eigenstates $|d_{z^2}, \pm\rangle$ with their corresponding eigenvalues $E_{\pm}(\mathbf{k})$ of $H_{eff}(\mathbf{k})$ are perturbatively good approximations for $|c, \pm, \mathbf{k}\rangle$ and $E_{c,\pm}(\mathbf{k})$ for evaluating Ω^{intra} in Eq.D-2.

In fact, such an effective model can be obtained by treating intra- $|d_{z^2}\rangle$ -orbital terms in $H_{tot}(\mathbf{k})$ (Eq.D-1) as

an unperturbed Hamiltonian, while the coupling between $|d_{z^2}\rangle$ and the remote $|d_{x^2-y^2} + id_{xy}\rangle$ -states (which are predominantly in the valence band) in Eq.D-1 are regarded as perturbations. Based on generalized second-order perturbation theory, we project contributions from the $|d_{x^2-y^2} + id_{xy}\rangle$ -states onto the subspace of $\{|d_{z^2}, \uparrow\rangle, |d_{z^2}, \downarrow\rangle\}$ -states and obtain the effective two-band Hamiltonian (for $k \sim 0 - 0.06 \text{ \AA}^{-1}$):

$$\begin{aligned}
H_{eff}(\mathbf{k}) &= \left(\frac{\Delta V_F^2}{\Delta^2 - \lambda^2} k^2 \right) \sigma_0 + \alpha_{so} \mathbf{k} \times \boldsymbol{\sigma}_{\parallel} \\
&+ (\beta_0 + \beta_1 k^2 + \frac{\lambda V_F^2}{\Delta^2 - \lambda^2} k^2) \sigma_z.
\end{aligned} \tag{D-3}$$

Here, the σ -Pauli matrices act on spins of d_{z^2} -orbitals, and $k^2 = k_x^2 + k_y^2$. For simplicity, we drop all constant terms in Eq.D-3 which have no contributions to Berry curvatures. Notably, the form of H_{eff} in Eq.D-3 is exactly the same as H_0 (Eq.1 of the main text), which is derived based on the C_{3v} point group symmetry. In particular, by defining $\beta_1 \equiv \beta_1' + \lambda V_F^2 / (\Delta^2 - \lambda^2)$, we identify the σ_z -term in H_{eff} is exactly the Ising SOC term discussed in Eq.1 of the main text. Thus, the Berry curvature derived from H_{eff} , which serves as a perturbative approximation of Ω^{intra} , is exactly the spin-type Berry curvature Ω_{spin} discussed in the main text. Therefore, we conclude that $\Omega^{intra}(\mathbf{k}) \approx \Omega_{spin}(\mathbf{k})$ throughout the regime explored in this work.

Next, we show that $\Omega^{inter} \approx \Omega_{orb}$ is also true for $k \sim 0 - 0.06 \text{ \AA}^{-1}$. By the same reasoning above, it is straightforward to see that the weight of the $|d_{z^2}\rangle$ -orbitals in the valence band states is also on the order of $V_F^2 k^2 / \Delta^2 < 2\%$ within the range $k \sim 0 - 0.06 \text{ \AA}^{-1}$. Thus, to evaluate the inter-band contribution Ω^{inter} , the eigenstates $|c, -, \mathbf{k}\rangle$ and $|v, \pm, \mathbf{k}\rangle$ can be well approximated as $|c, -, \mathbf{k}\rangle \approx |d_{z^2}, -, \mathbf{k}\rangle$ and $|v, \pm, \mathbf{k}\rangle \approx |d_{x^2-y^2} + id_{xy}, \pm, \mathbf{k}\rangle$. We note that due to Rashba SOCs, the out-of-plane spin of eigenstates in the conduction band is no longer conserved. Thus, we have in general $|d_{z^2}, -, \mathbf{k}\rangle = s_1(\mathbf{k}) |d_{z^2}, \uparrow\rangle + s_2(\mathbf{k}) |d_{z^2}, \downarrow\rangle$, and the \mathbf{k} -dependent coefficients s_1, s_2 need to be determined by diagonalizing $H_{eff}(\mathbf{k})$. However, by observing that $\Delta \gg \lambda \gg \beta_0, \beta_1 k^2$ in the regime of our interest, we have $E_{c,-}(\mathbf{k}) - E_{v,\pm}(\mathbf{k}) \approx \Delta$. With $|d_{x^2-y^2} + id_{xy}, +(-), \mathbf{k}\rangle = |d_{x^2-y^2} + id_{xy}, \uparrow(\downarrow), \mathbf{k}\rangle$, we have:

$$\begin{aligned}
\Omega_{c,-}^{inter}(\mathbf{k}) &= i \sum_{m=\pm} \frac{\langle c, -, \mathbf{k} | \hat{v}_x | v, m, \mathbf{k} \rangle \langle v, m, \mathbf{k} | \hat{v}_y | c, -, \mathbf{k} \rangle - c.c.}{(E_{c,-}(\mathbf{k}) - E_{v,m}(\mathbf{k}))^2} \\
&\approx -(|s_1(\mathbf{k})|^2 \frac{V_F^2}{\Delta^2} + |s_2(\mathbf{k})|^2 \frac{V_F^2}{\Delta^2}) \\
&= -\frac{V_F^2}{\Delta^2}
\end{aligned} \tag{D-4}$$

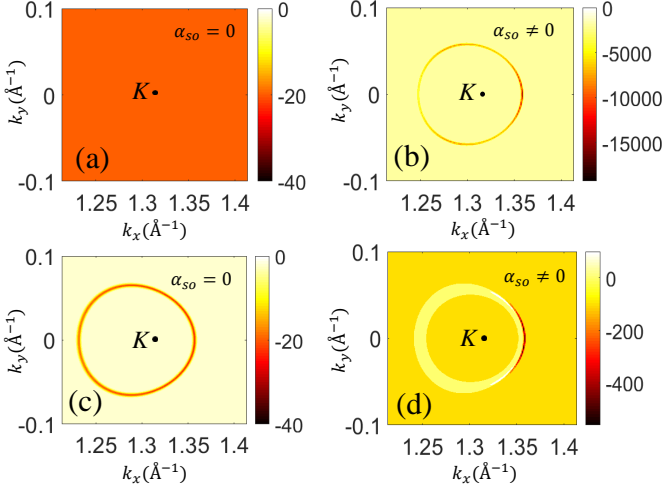


FIG. D-1: Effects of Ω_{spin} on total Berry curvature profiles in strained MoSSe. Color bar indicates the value of total Berry curvature in units of \AA^2 . (a)-(b) Profiles of Ω_{tot} of the lower conduction band $n = c, -$ throughout the neighborhood of K in (a) strained MoS2 without Ω_{spin} and (b) strained MoSSe with Ω_{spin} . (c)-(d) Profiles of Ω_{tot} along Fermi contour enclosing the K -point at $E_F = 1.467$ eV in (c) strained MoS2 without Ω_{spin} and (d) strained MoSSe with Ω_{spin} .

Note that in the last step we used the normalization condition $|s_1|^2 + |s_2|^2 = 1$. As shown in Ref.[17], in the limit $V_F k \ll \Delta$, Ω_{orb} is almost a constant with value $\frac{V_F^2}{\Delta^2}$ (a uniform momentum space profile in the neighborhood of K). It is clear that $V_F k \ll \Delta$ holds in the range $k \sim 0 - 0.06 \text{\AA}^{-1}$ of our interest. Thus, we have $\Omega_{inter} \approx \Omega_{orb}$.

Based on our detailed analysis above, we conclude that $\Omega_{tot} \approx \Omega_{spin} + \Omega_{orb}$ holds throughout the regime explored in our work. We note that this relation would fail when $V_F k \sim \Delta$. However, this would require the Fermi level to exceed 100 meVs[26] which goes way beyond the regime of our interest.

According to Fig.A-1, $|\Omega_{spin}| \sim 10^4 \text{\AA}^2$ near the band anti-crossing points, while $|\Omega_{orb}| \sim 10 \text{\AA}^2$ [17]. Thus, Ω_{spin} strongly dominates over Ω_{orb} near the band anti-crossing points. Based on our discussions in subsection A, the relation $\Omega_{tot} \approx \Omega_{spin} + \Omega_{orb}$ implies that the behavior of Ω_{tot} is essentially governed by Ω_{spin} in the regime

of our interest. In this section, we explicitly demonstrate how the dominance of Ω_{spin} gives rise to strongly enhanced Berry dipole of order 1\AA near the band anti-crossing points as shown in Fig.2-3 of the main text.

First, to demonstrate how Ω_{spin} significantly enhances the total Berry curvature in strained MoSSe, we plot the profiles of Ω_{tot} of the lower conduction band $n = c, -$ throughout the neighborhood of K as shown in Fig.D-1a-b. In Fig.D-1a, the Rashba SOC is absent ($\alpha_{so} = 0$), thus $\Omega_{spin} = 0$ according to Eq.2 of the main text. In this case, the magnitude of Ω_{tot} remains almost a constant at $\sim 10 \text{\AA}^2$. Notably, as we discussed in subsection A, the profile of Ω_{tot} is approximately a uniform function near K due to the fact that $V_F k \ll \Delta$ [17].

In contrast, when Rashba SOC is present, the maximum amplitude of Ω_{tot} is significantly enhanced near the band anti-crossing points due to the presence of Ω_{spin} (Fig.D-1b). Note that the magnitude of Ω_{tot} is also on the order of 10^4\AA^2 , being consistent with the relation: $\Omega_{tot} \approx \Omega_{spin} + \Omega_{orb}$. Importantly, as the magnitude of Ω_{spin} changes dramatically as \mathbf{k} goes from K to the band anti-crossing points (Eq.2 of the main text), the profile of Ω_{tot} also becomes highly nonuniform in the neighborhood of K as explicitly shown in Fig.D-1b.

Second, to demonstrate how Ω_{spin} leads to strongly enhanced Berry dipole in strained MoSSe, we plot the Berry curvature profiles *along a fixed Fermi contour enclosing the K -point* (i.e., only momentum states at a given Fermi energy E_F are considered) as shown in Fig.D-1c-d. This provides a physical picture of a Berry dipole according to Eq.4 of the main text, which can be regarded as a manifestation of its Fermi liquid property. As shown in Fig.D-1c, when Ω_{spin} is absent, the total Berry curvature Ω_{tot} is also approximately a constant along the Fermi contour due to the uniform Berry curvature profile throughout the neighborhood of K (Fig.D-1). As the Berry dipole is given by the sum of products between Fermi velocity and Berry curvature at each \mathbf{k} along the Fermi surface (Eq.4 of the main text), the contributions from all states \mathbf{k} in Fig.D-1c almost cancel each other because their Berry curvatures are roughly the same while their velocities almost sum to zero.

In sharp contrast, with the same Fermi contour in Fig.D-1c, due to the highly nonuniform profile of Ω_{tot} in Fig.D-1b, Ω_{tot} also changes drastically along the Fermi contour as shown in Fig.D-1d. Note that due to the bro-

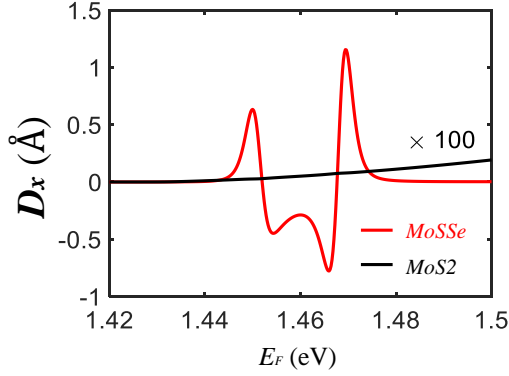


FIG. D-2: Gate-dependence of Berry curvature dipole D_x in strained MoS₂ (black solid line) and strained MoSSe (red solid line) with $u_{xx} = 4\%$. Note that D_x in strained MoS₂ is multiplied by 100 times so that the values can be visible on the scale of 0.5\AA . For direct comparison, all parameters used for calculating both curves are set to be the same except that $\alpha_{so} \neq 0$ for MoSSe.

ken C_3 symmetry by strain, the Berry curvature profile is no longer three-fold invariant about K . Particularly, with the choice of Fermi energy lying close to hot spots of Ω_{spin} associated with the right-movers, the Berry curvature along the Fermi contour enclosing K is concentrated preferentially on the right hand side of K (Fig.D-1d). In this case, the largely imbalanced Berry curvature contributions from right-movers and left-movers lead to a large Berry dipole according to Eq.4 of the main text.

We now explicitly demonstrate the enhancement of Berry dipole due to Ω_{spin} . We calculate the Berry dipole for strained conventional MoS₂ without Rashba SOC's for a direct comparison with strained MoSSe with Rashba SOC's. As shown clearly in Fig.D-2, the magnitude of D_x in MoS₂ is only of the order $1 \times 10^{-3}\text{\AA}$ in the regime where D_x is of order 1\AA in strained MoSSe. Thus, D_x is strongly enhanced by 3 orders of magnitude in the Fermi level regime $E_F \sim 1.44 - 1.48$ eV due to the presence of Ω_{spin} . We note by passing that the optimal value for D_x in strained MoS₂ (with contributions from Ω_{orb} only) can be as large as $\sim 0.01\text{\AA}$ at a higher E_F which goes beyond the regime considered here. Thus, the optimal value is also enhanced by 2 orders of magnitude due to Ω_{spin} .

Appendix E: Berry curvature dipole in other strained polar TMDs

Here, we discuss nonlinear Hall effects in other strained polar TMDs. First, as we mentioned in the main text, our prediction of large Berry dipole generally applies to the whole class of moly-based polar TMDs. This is due to the fact that in all conventional moly-based TMDs, there readily exists a band crossing within the two electron bands[26]. As a result, once Rashba SOC's are turned on, the band crossing points are gapped out, leading to

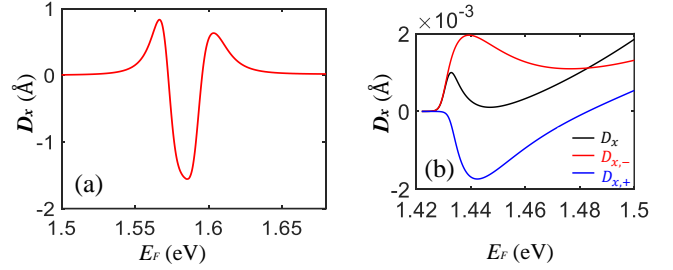


FIG. E-1: Gate-dependence of Berry curvature dipole D_x in (a) strained MoSeTe with $u_{xx} = 2\%$ and (b) strained WSeTe with $u_{xx} = 4\%$.

band-anticrossings where Berry curvature hot spots can emerge.

To explicitly demonstrate the generality of the mechanism above, we calculate the gate-dependence of Berry dipole of another moly-based TMD material, MoSeTe, as shown in Fig.E-1a under uniaxial strain $u_{xx} = 2\%$. The tight-binding model used for MoSeTe is exactly the same as the one presented in Section II and III, with the parameters for MoSeTe listed in Table III and IV. The SOC tight-binding parameters for MoSeTe are given by $\alpha_0 = 1.2$ meV, and $\beta_{so} = -15$ meV. Clearly, D_x in MoSeTe has the same qualitative gate-dependent features as MoSSe under similar strain $u_{xx} \sim 2\%$ (Fig.3 of the main text). Notably, the optimal value of D_x in MoSeTe is also of the order 1\AA .

On the other hand, as we pointed out in the main text, in tungsten(W)-based 2H-TMDs, the SOC-induced Berry curvature Ω_{spin} can also modify the total Berry curvature profile near the conduction band minimum. However, since there is no band anti-crossing in W-based materials, the Berry curvature profile is much less nonuniform compared to the moly-based case and the Berry curvature dipole is expected to be less strongly enhanced. Here, using a specific example of W-based polar TMD candidate WSeTe, we demonstrate this fact by calculating the Berry curvature dipole under the same uniaxial strain $u_{xx} = 4\%$ as in Fig.2 of the main text. For W-based materials, the Ising SOC in the conduction band is set to be $\beta_0 \approx 20$ meV[26]. Strong Rashba splitting ~ 50 meV has also been predicted for WSeTe[20], and the fitted parameter in the tight-binding model is set to be $\alpha_0 \approx 45$ meV according to previous works[22]. For simplicity, the other parameters are set to be the same as those presented in Table III and Table IV.

The Berry curvature dipole D_x as a function of the Fermi energy E_F for strained WSeTe is shown in Fig.E-1b. Clearly, the Berry curvature dipole is also on the order of $1 \times 10^{-3}\text{\AA}$, comparable to the case of conventional 2H-TMDs while much smaller than the values in strained MoSSe (Fig.2 of the main text). However, due to the fact that Ω_{spin} causes the two bands to carry opposite Berry curvatures, the contributions $D_{x,-}/D_{x,+}$ from lower/upper bands to D_x also have different signs

as shown in Fig.E-1b, which results in some cancellation effects as the upper band gets filled (signified by the point in the $D_x - E_F$ curves where D_x starts to deviate from

$D_{x,-}$). While certain non-trivial gate-dependence in D_x is also found, the sign of D_x is not switched as in the case of MoSSe (Fig.2 & 3 of the main text).

-
- [1] Xiao, D., Chang, M. and Niu, Q. *Berry phase effects on electronic properties*. Rev. Mod. Phys. **82**, 1959-2007 (2010).
- [2] Naoto Nagaosa, Jairo Sinova, Shigeki Onoda, A. H. MacDonald, and N. P. Ong *Anomalous Hall effect* Rev. Mod. Phys. **82**, 1539 (2010).
- [3] L. D. Landau, E. M. Lifshitz, and L. P. Pitaevskii, in *Statistical Physics, Course of Theoretical Physics Vol. 5*, 3rd. ed. (Pergamon Press, Oxford, 1999)
- [4] Dimitrie Culcer, Allan MacDonald, and Qian Niu, *Anomalous Hall effect in paramagnetic two-dimensional systems*. Phys. Rev. B **68**, 045327 (2003).
- [5] Inti Sodemann and Liang Fu, *Quantum Nonlinear Hall Effect Induced by Berry Curvature Dipole in Time-Reversal Invariant Materials*, Phys. Rev. Lett. **115**, 216806 (2015).
- [6] J. Lee, Z. Wang, H. Xie, K. F. Mak, J. Shan, *Valley Magnetoelectricity in Single-Layer MoS₂*, Nature Materials, doi:10.1038/nmat4931 (2017).
- [7] Hiroki Isobe, Su-Yang Xu, and Liang Fu, *High-frequency rectification via chiral Bloch electrons*, arXiv:1812.08162 (2018).
- [8] Tony Low, Yongjin Jiang and Francisco Guinea, *Topological currents in black phosphorus with broken inversion symmetry*, Phys. Rev. B **92**, 235447 (2015).
- [9] E. Deyo, L.E. Golub, E.L. Ivchenko, B. Spivak, *Semiclassical theory of the photogalvanic effect in non-centrosymmetric systems*, arXiv:0904.1917 (2009).
- [10] Lukas Muechler, A. Alexandradinata, Titus Neupert, and Roberto Car, *Topological Nonsymmorphic Metals from Band Inversion*, Phys. Rev. X **6**, 041069 (2016).
- [11] Jih-Shih You, Shiang Fang, Su-Yang Xu, Efthimios Kaxiras, and Tony Low, *Berry curvature dipole current in the transition metal dichalcogenides family*, Phys. Rev. B **98**, 121109(R) (2018).
- [12] Zhang, Y., Brink, J. V. d., Felser, C. and Yan, B. *Electrically tuneable nonlinear anomalous Hall effect in two-dimensional transition-metal dichalcogenides WTe₂ and MoTe₂* 2D Materials 5, 044001 (2018).
- [13] Qiong Ma, Su-Yang Xu, Huitao Shen, David MacNeill, Valla Fatemi, Tay-Rong Chang, Andrs M. Mier Valdivia, Sanfeng Wu, Zongzheng Du, Chuang-Han Hsu, Shiang Fang, Quinn D. Gibson, Kenji Watanabe, Takashi Taniguchi, Robert J. Cava, Efthimios Kaxiras, Hai-Zhou Lu, Hsin Lin, Liang Fu, Nuh Gedik & Pablo Jarillo-Herrero *Observation of the nonlinear Hall effect under time-reversal-symmetric conditions*, Nature, DOI: 10.1038/s41586-018-0807-6 (2018).
- [14] Kaifei Kang, Tingxin Li, Egon Sohn, Jie Shan, Kin Fai Mak, *Observation of the nonlinear anomalous Hall effect in 2D WTe₂*, Nature Materials, DOI: 10.1038/s41563-019-0294-7 (2019).
- [15] Z. Z. Du, C. M. Wang, Hai-Zhou Lu, and X. C. Xie, *Band Signatures for Strong Nonlinear Hall Effect in Bilayer WTe₂*, Phys. Rev. Lett. **121**, 266601 (2018).
- [16] P. Olbrich, L. E. Golub, T. Herrmann, S. N. Danilov, H. Plank, V. V. Belkov, G. Mussler, Ch. Weyrich, C. M. Schneider, J. Kampmeier, D. Grutzmacher, L. Plucinski, M. Eschbach, and S. D. Ganichev, Phys. Rev. Lett. **113**, 096601 (2014).
- [17] D. Xiao, G. Liu, W. Feng, X. Xu, W. Yao, *Coupled spin and valley physics in monolayers of MoS₂ and other group-VI dichalcogenides*. Phys. Rev. Lett. **108**, 196802 (2012).
- [18] Mak, K.F., McGill, K.L., Park, J. and McEuen, P.L. *The valley Hall effect in MoS₂ transistors*. Science **344**, 1489-1492 (2014).
- [19] J. M. Lu, O. Zheliuk, I. Leermakers, N. F. Q. Yuan, U. Zeitler, K. T. Law, and J. T. Ye, *Evidence for two-dimensional Ising superconductivity in gated MoS₂*, Science **350**, 1353-1357 (2015).
- [20] Qun-Fang Yao, Jia Cai, Wen-Yi Tong, Shi-Jing Gong, Ji-Qing Wang, Xiangang Wan, Chun-Gang Duan, and J. H. Chu, *Manipulation of the large Rashba spin splitting in polar two-dimensional transition-metal dichalcogenides* Phys. Rev. B **95**, 165401 (2017).
- [21] Y. C. Cheng, Z. Y. Zhu, M. Tahir, and U. Schwingenschlogl, Europhys. Lett. **102**, 57001 (2013).
- [22] Benjamin T. Zhou, Katsuhisa Taguchi, Yuki Kawaguchi, Yukio Tanaka, K. T. Law, *Spin-orbit-coupling induced valley Hall effects in transition-metal dichalcogenides*, Communications Physics **2**, 26 (2019).
- [23] K. Taguchi, B. T. Zhou, Y. Kawaguchi, Y. Tanaka, and K. T. Law, *Valley Edelstein effect in monolayer transition-metal dichalcogenides*, Phys. Rev. B **98**, 035435 (2018).
- [24] Ang-Yu Lu, Hanyu Zhu, Jun Xiao, Chih-Piao Chuu, Yimo Han, Ming-Hui Chiu, Chia-Chin Cheng, Chih-Wen Yang, Kung-Hwa Wei, Yiming Yang, Yuan Wang, Dimosthenis Sokaras, Dennis Nordlund, Peidong Yang, David A. Muller, Mei-Yin Chou, Xiang Zhang & Lain-Jong Li, *Janus monolayers of transition metal dichalcogenides*. Nat. Nanotech. **12**, 744749 (2017).
- [25] Jing Zhang et al., *Janus Monolayer Transition-Metal Dichalcogenides*. ACS Nano, **11**(8), 81928198 (2017).
- [26] Liu, G.-B., Shan, W.-Y., Yao, Y., Yao, W. & Xiao, D. *Three-band tight-binding model for monolayers of group-VIB transition metal dichalcogenides*, Phys. Rev. B **88**, 085433 (2013).
- [27] N. F. Q. Yuan, K. F. Mak, and K. T. Law, *Possible Topological Superconducting Phases of MoS₂*, Phys. Rev. Lett. **113**, 097001 (2014).
- [28] Yuan, H. T. et al. *Zeeman-type spin splitting controlled by an electric field*, Nat. Phys. **9**, 563-569 (2013).
- [29] Z. Y. Zhu, Y. C. Cheng, and U. Schwingenschlogl *Giant spin-orbit-induced spin splitting in two-dimensional transition-metal dichalcogenide semiconductors* Phys. Rev. B **84**, 153402 (2011).
- [30] A. Kormanyos, V. Zolyomi, N. D. Drummond, P. Rakyta, G. Burkard and V. I. Falko, *Monolayer MoS₂: Trigonal warping, the Γ valley, and spin-orbit coupling effects*. Phys. Rev. B **88**, 045416 (2013).

- [31] K. Kośmider, J. W. González and J. Fernández-Rossier, *Large spin splitting in the conduction band of transition metal dichalcogenide monolayers*, Phys. Rev. B **88**, 245436 (2013).
- [32] E. I. Rashba, *Symmetry of bands in wurzite-type crystals. 1. Symmetry of bands disregarding spin-orbit interaction*, Sov. Phys. Solid. State **1**, 368 (1959).
- [33] B. Andrei Bernevig, Taylor L. Hughes, Shou-Cheng Zhang, *Quantum Spin Hall Effect and Topological Phase Transition in HgTe Quantum Wells*, Science **314**, 5806 (2006).
- [34] X.L. Qi, Y. S. Wu, and S.C. Zhang, *General theorem relating the bulk topological number to edge states in two-dimensional insulators*, Phys. Rev. B **74**, 045125 (2006).
- [35] G. E. Volovik, *The Universe in a Helium Droplet* (Oxford University Press, USA, 2003).
- [36] Shiang Fang, Stephen Carr, Miguel A. Cazalilla, and Efthimios Kaxiras, *Electronic structure theory of strained two-dimensional materials with hexagonal symmetry* Phys. Rev. B **98**, 075106 (2018).
- [37] S. Hemour and K. Wu, Proc. IEEE **102**, 1667 (2014).
- [38] K. V. Selvan and M. S. Mohamed Ali, Renew. Sust. Energ. Rev. **54**, 1035 (2016).
- [39] Jieun Lee, Kin Fai Mak and Jie Shan, *Electrical control of the valley Hall effect in bilayer MoS₂ transistors*, Nat. Nanotech. **11**, 421425 (2016).
- [40] Zefei Wu et al., *Intrinsic valley Hall transport in atomically thin MoS₂*, Nat. Commun. **10**, 611 (2019).
- [41] E. J. König, M. Dzero, A. Levchenko, and D. A. Pesin, Phys. Rev. B **99**, 155404 (2019).
- [42] S. Nandy, I. Sodemann, arXiv:1901.04467 (2019).
- [43] Z. Z. Du, C. M. Wang, Shuai Li, Hai-Zhou Lu & X. C. Xie, Nat. Commun. **10**, 3047 (2019).
- [44] Cong Xiao, Z. Z. Du, Qian Niu, arXiv:1907.00577 (2019).